



AFRL-RZ-WP-TR-2010-2203

**SPECTROSCOPIC INVESTIGATION OF THE ARGON
METASTABLE STATE THROUGH OPTICAL EMISSION
FROM PULSED ARGON DISCHARGE**

Jared A. Miles and Steven F. Adams

**Energy and Power Systems Branch
Energy/Power/Thermal Division**

**JULY 2010
Interim Report**

Approved for public release; distribution unlimited.

See additional restrictions described on inside pages

STINFO COPY

**AIR FORCE RESEARCH LABORATORY
PROPULSION DIRECTORATE
WRIGHT-PATTERSON AIR FORCE BASE, OH 45433-7251
AIR FORCE MATERIEL COMMAND
UNITED STATES AIR FORCE**

NOTICE AND SIGNATURE PAGE

Using Government drawings, specifications, or other data included in this document for any purpose other than Government procurement does not in any way obligate the U.S. Government. The fact that the Government formulated or supplied the drawings, specifications, or other data does not license the holder or any other person or corporation; or convey any rights or permission to manufacture, use, or sell any patented invention that may relate to them.

This report was cleared for public release by the USAF 88th Air Base Wing (88 ABW) Public Affairs (AFRL/PA) Office and is available to the general public, including foreign nationals. Copies may be obtained from the Defense Technical Information Center (DTIC) (<http://www.dtic.mil>).

AFRL-RZ-WP-TR-2010-2203 HAS BEEN REVIEWED AND IS APPROVED FOR PUBLICATION IN ACCORDANCE WITH THE ASSIGNED DISTRIBUTION STATEMENT.

*//Signature//

STEVEN F. ADAMS
Program Manager
Energy and Power Systems Branch
Energy/Power/Thermal Division
Propulsion Directorate

//Signature//

JOSEPH A. WEIMER
Chief
Energy and Power Systems Branch
Energy/Power/Thermal Division
Propulsion Directorate

This report is published in the interest of scientific and technical information exchange, and its publication does not constitute the Government's approval or disapproval of its ideas or findings.

*Disseminated copies will show “//Signature//” stamped or typed above the signature blocks.

REPORT DOCUMENTATION PAGE				Form Approved OMB No. 0704-0188	
<p>The public reporting burden for this collection of information is estimated to average 1 hour per response, including the time for reviewing instructions, searching existing data sources, gathering and maintaining the data needed, and completing and reviewing the collection of information. Send comments regarding this burden estimate or any other aspect of this collection of information, including suggestions for reducing this burden, to Department of Defense, Washington Headquarters Services, Directorate for Information Operations and Reports (0704-0188), 1215 Jefferson Davis Highway, Suite 1204, Arlington, VA 22202-4302. Respondents should be aware that notwithstanding any other provision of law, no person shall be subject to any penalty for failing to comply with a collection of information if it does not display a currently valid OMB control number. PLEASE DO NOT RETURN YOUR FORM TO THE ABOVE ADDRESS.</p>					
1. REPORT DATE (DD-MM-YY) July 2010		2. REPORT TYPE Interim		3. DATES COVERED (From - To) 08 April 2009 – 22 July 2010	
4. TITLE AND SUBTITLE SPECTROSCOPIC INVESTIGATION OF THE ARGON METASTABLE STATE THROUGH OPTICAL EMISSION FROM PULSED ARGON DISCHARGE				5a. CONTRACT NUMBER In-house	
				5b. GRANT NUMBER	
				5c. PROGRAM ELEMENT NUMBER 62203F	
6. AUTHOR(S) Jared A. Miles and Steven F. Adams				5d. PROJECT NUMBER 3145	
				5e. TASK NUMBER 13	
				5f. WORK UNIT NUMBER 31451314	
7. PERFORMING ORGANIZATION NAME(S) AND ADDRESS(ES) Energy and Power Systems Branch (AFRL/RZPE) Energy/Power/Thermal Division Air Force Research Laboratory, Propulsion Directorate Wright-Patterson Air Force Base, OH 45433-7251 Air Force Materiel Command, United States Air Force				8. PERFORMING ORGANIZATION REPORT NUMBER AFRL-RZ-WP-TR-2010-2203	
9. SPONSORING/MONITORING AGENCY NAME(S) AND ADDRESS(ES) Air Force Research Laboratory Propulsion Directorate Wright-Patterson Air Force Base, OH 45433-7251 Air Force Materiel Command United States Air Force				10. SPONSORING/MONITORING AGENCY ACRONYM(S) AFRL/RZPE	
				11. SPONSORING/MONITORING AGENCY REPORT NUMBER(S) AFRL-RZ-WP-TR-2010-2203	
12. DISTRIBUTION/AVAILABILITY STATEMENT Approved for public release; distribution unlimited.					
13. SUPPLEMENTARY NOTES PAO Case Number: 88ABW-2010-4239, Clearance Date: 09 Aug 2010.					
14. ABSTRACT A plasma diagnostic technique has been experimentally demonstrated where optical emission measurements of relative intensities of spectral lines in the violet range were combined with available electron-impact cross sections to yield absolute Ar metastable species concentration. An enabling factor of this analysis was that the electron excitation pattern was quite different between the Ar ground state and the metastable state. The result of this pattern was that the optical spectrum was unique depending on whether the emission was generated by direct excitation from the ground state, or by stepwise excitation from one of the metastable states. This study has shown that a model combining Ar excitation cross sections can fit the experimental spectral distributions by varying the ratio of the metastable state density and the E/N within the discharge. The absolute density obtained through optical emission spectroscopy was compared to measurements using laser diode absorption in order to confirm the results.					
15. SUBJECT TERMS argon, glow discharge, optical emission, spectroscopy, metastable					
16. SECURITY CLASSIFICATION OF:			17. LIMITATION OF ABSTRACT: SAR	18. NUMBER OF PAGES 76	19a. NAME OF RESPONSIBLE PERSON (Monitor) Steven F. Adams 19b. TELEPHONE NUMBER (Include Area Code) N/A
a. REPORT Unclassified	b. ABSTRACT Unclassified	c. THIS PAGE Unclassified			

TABLE OF CONTENTS

SECTION	PAGE
LIST OF FIGURES	v
LIST OF TABLES	vii
ACKNOWLEDGMENTS	viii
1 Summary	1
2 Introduction	2
3 Theory	5
3.1 Argon Electronic Structure	5
3.2 Radiative Transitions in Argon	10
3.3 Electron Impact Cross Sections	12
3.4 Electron Energy Distribution Function	13
3.5 Optical Emission Intensity	14
3.6 Diode Laser Absorption Spectroscopy	15
4 Previous Work	19
4.1 Argon Metastable Density Measurements	19
4.1.1 Optical Emission Spectroscopy	19
4.1.2 Laser Absorption	20
4.2 Argon Electron Impact Cross Sections	20
5 Experimental	23
5.1 Pulsed DC Discharge	23
5.1.1 Discharge Tube and Vacuum System	23
5.1.2 Power Supply	24

5.1.3	Pressure and Flow Measurement	25
5.1.4	Electric Field Measurement	26
5.1.5	Optical Emission Measurement	27
5.2	Absorption	29
6	Results and Discussion	35
6.1	Experimental Emission Spectra	35
6.2	Simulated Emission Spectra	37
6.2.1	Simulated Spectrum During Breakdown	39
6.2.2	Simulated Spectrum During Discharge	42
6.2.3	Simulated Spectrum After Discharge	44
6.3	Diode Laser Absorption	47
6.3.1	Absorption During Breakdown	48
6.3.2	Absorption During Discharge	48
6.3.3	Absorption After Discharge	49
6.4	Relation of Line-Intensity Ratio, Metastable Density, and E/N	49
7	Conclusion	52
	REFERENCES	54
	APPENDIX	57
	LIST OF SYMBOLS	62

LIST OF FIGURES

FIGURE		PAGE
1	Jared Miles collecting optical emission from a pulsed Ar gas discharge . .	3
2	Pulsed discharge voltage (solid line) and metastable density (dashed line)	23
3	Discharge tube and vacuum components configuration	24
4	Optical Emission measurement set Up	25
5	Voltage and current waveforms for one pulse	26
6	Voltage probe measurements	27
7	Difference in voltage probe measurements	28
8	Diode laser absorption experimental set up	30
9	Transmission ratio vs time	31
10	Transmission (solid line) and etalon signal (dotted line) vs relative Frequency	32
11	Gaussian fit (solid line) and $\ln(I_o/I)$ (\times) for $1s_3 \rightarrow 2p_2$ transition	33
12	Gaussian fit (solid line) and $\ln(I_o/I)$ (\times) for $1s_5 \rightarrow 2p_7$ transition	34
13	Column density measurements	34
14	Times where emission was recorded	35
15	Emission during breakdown	36
16	Emission during discharge	36
17	Emission after discharge	37

18	Cross sections used in theoretical fit	39
19	Emission at time (i) and simulated fit (\times)	40
20	$\epsilon f(\epsilon)$ at time (i) and optical cross sections	41
21	Emission at time (ii) and simulated fit (\times) with error bars	42
22	$\epsilon f(\epsilon)$ at time (ii) and optical cross sections	44
23	Emission at time (iii) with simulated fit (\times)	45
24	$\epsilon f(\epsilon)$ at time (iii) and optical cross sections	46
25	Temporal profile of absorption for the $1s_5 \rightarrow 2p_7$ transition	47
26	Graphical representation of line-intensity ratio, metastable density, and E/N	50

LIST OF TABLES

TABLE		PAGE
1	Energy levels	9
2	Optical cross sections for transitions originating from the ground state . .	58
3	Coefficient values for $\sigma_{mn}(\epsilon)$	59
4	Optical cross sections for transitions originating from metastable states .	60
5	Coefficient values for $\sigma_{mn}^*(\epsilon)$ originating from the Ar $1s_5$ Metastable state	60
6	Coefficient values for $\sigma_{mn}^*(\epsilon)$ originating from the Ar $1s_3$ Metastable state	61

ACKNOWLEDGMENTS

First of all we would like to thank technician Boyd Allen Tolson for all of his masterful and versatile assistance in the laboratory. We would also like to acknowledge Mike Ray for the craftsmanship he displayed in fabricating the glassware used in this project. Quality assistance was provided by students throughout this project including Adam Laber, Dustin Fisher, John Blessington, Amber Hensley, Luke Sobota, and Sean Nuzum. We would like to thank Dr. Bish Ganguly and Dr. Robert Leiweke for granting us access to their diode laser absorption experiment. We are also appreciative of Dr. Jerry Clark, Dr. James Williamson, Dr. Vladimir Demidov, Dr. Charles DeJoseph, Jr., and Dr. Jason Deibel for their fine consultations concerning this work.

CHAPTER 1

Summary

A plasma diagnostic technique has been experimentally demonstrated where optical emission measurements of relative intensities of spectral lines in the violet range were combined with available electron-impact cross sections to yield absolute Ar metastable species concentration. An enabling factor of this analysis was that the electron excitation pattern was quite different between the Ar ground state and the metastable state. The result of this pattern was that the optical spectrum was unique depending on whether the emission was generated by direct excitation from the ground state, or by stepwise excitation from one of the metastable states. This study has shown that a model combining Ar excitation cross sections can fit the experimental spectral distributions by varying the ratio of the metastable state density and the E/N within the discharge. The absolute density obtained through optical emission spectroscopy was compared to measurements using laser diode absorption in order to confirm the results.

CHAPTER 2

Introduction

Plasma, also known as the fourth state of matter, exists naturally in our universe in stars and within the interstellar medium, but also occurs naturally on earth in our ionosphere, auroras, lightning, and fire. Artificial sources can also generate plasma by a electrical gas discharge [1]. In a typical low pressure gas discharge, energy provided by an applied electric field produces collisions between free electrons and neutrals, causing excitation and ionization of the neutrals that sustain the weakly ionized state of the gas. The spatial distribution of electrons and negatively and positively charged ions throughout the gas allows it to be electrically conductive, while the shielding effects of the charge distribution retard charge recombination and help the plasma to be self-sustaining [2].

In recent years, a variety of plasma techniques are finding wide application in both research and production including surface processing, radiation sources, fluorescent lighting, plasma displays, biomedical applications, electronic switches, and space thrusters [3]. The semiconductor industry uses plasma sources to etch and deposit material using the highly energetic and reactive atoms that plasmas produce [4]. Fusion power research investigates how ultra hot plasmas fuse deuterium and tritium together in hopes that a sustainable energy source can someday be developed [5]. The recent consumer trend of replacing incandescent light bulbs with compact fluorescence lamps is driven by the efficiency of plasma generated visible and ultraviolet light which, when combined with fluorescent lamp coatings, can generate a very efficient and long-life visible light source with sun-like color rendering [6].

Noble gases, which have high ionization energies, are often used in gas discharges as buffer gases, since they are almost always chemically inactive. Argon (Ar) is often used over heavier gases like Xenon and Krypton because it is more abundant and cheaper than the heavier noble gases. Because of its many applications as a buffer gas, Ar plasma has been extensively studied. Physical parameters of the energetic species in an Ar plasma are often investigated, including electron and ion temperature, electron and ion density, and the density of electronically excited atoms [7]. These parameters can be studied using various electrical and optical diagnostic tools.

A better understanding of the origin of these physical properties within an Ar gas discharge and kinetic processes that create the Ar plasma would lead to improved optimization techniques for gas discharge sources and possibly some new applications. The non-equilibrium nature of the plasma discharge, with the electrons having a much higher kinetic energy than neutral species, makes it difficult to theoretically predict the densities of the charged and neutral species in the discharge and the resulting chemistry [2]. It has been the main objective of this effort to further the understanding of electron impact excitation within a low pressure Ar discharge and its influence on the generation of excited species and optical emission. The ultimate goal of this work would be the development

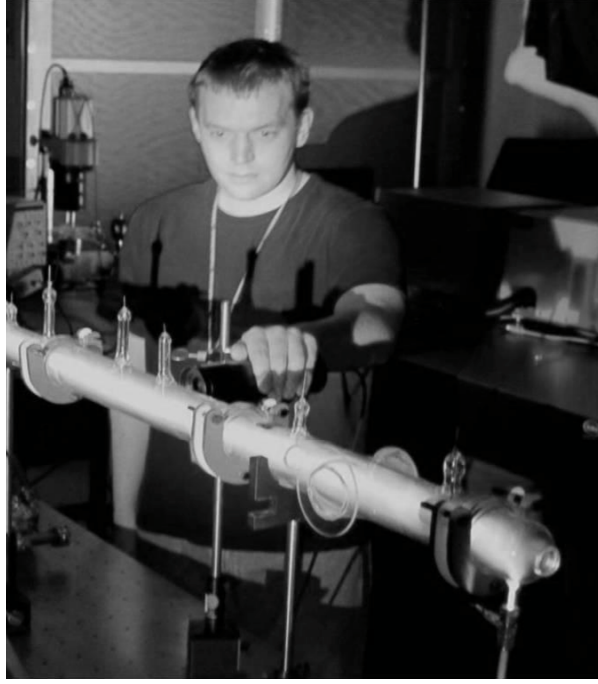


Figure 1: Jared Miles collecting optical emission from a pulsed Ar gas discharge

of a relatively simple optical emission technique that would provide accurate information on the concentration of important excited species within the Ar discharge.

Electronically excited atoms which, by the selection rules of quantum mechanics, do not readily radiate to lower energy states will often be characterized by a much longer lifetime than typical excited atoms. These long lived excited states are called metastable states and the corresponding excited atoms are sometimes referred to simply as metastables. In Ar, the lowest energy metastable states are denoted by $1s_5$ and $1s_3$ in Paschen notation [8]. The kinetic processes in Ar discharges are typically affected by the presence of these metastable states with their higher internal energy and slower rate of decay [7]. Ar metastable concentrations generally are relatively high among radical species because of their slow decay rate, but direct detection of these metastables by optical emission is challenging due to their non-radiative nature. It is possible, though, to determine some information concerning the Ar metastables by analyzing spectral features of optical processes that are indirectly affected by the presence of metastables [9]. Modeling of these indirect processes requires accurate physical data on properties such as electron impact excitation cross sections [10, 11] and electron energy distribution to determine the excitation rates leading to the optical emission spectrum. Laser diode absorption has also been successfully applied in measuring absolute Ar metastable densities, but this technique is more complex and expensive than optical emission measurements [12, 13]. This work will specifically focus on the spectral analysis of the emission of light in the violet region from an Ar discharge and its relationship to the density of electronically excited Ar in the metastable state.

A summary of the contents of this report and some comments on the structure are as follows. A theory chapter immediately follows this introduction and is a review of key physical concepts relating to Ar excitation and emission including electronic configurations, radiative transitions, excitation cross sections, and electron energy distribution. Laser absorption theory is also discussed since this technique is used to verify Ar metastable density measurements and assumptions made during emission experiments. This theory chapter precedes the chapter reviewing previous work, which is not a typical order, but is done here since the theory provides a general discussion of many of the issues that are mentioned in the previous works chapter. In the chapter reviewing previous work, earlier Ar metastable density measurements using both spectral analysis of the emission of light and laser diode absorption are discussed, as well as a review of previously measured Ar excitation cross sections. The experimental chapter describes the apparatuses used in both the optical emission measurements and laser diode absorption measurements and is followed by the results and discussion chapter and then the conclusion.

CHAPTER 3

Theory

3.1 Argon Electronic Structure

The core objective of this study involves analyzing optical emission due to electronic energy transfer within the Ar atom. Thus, it is essential to have an accurate model of the collective energy and angular momentum of the electrons that are bound to the Ar atom. Quantum mechanics provides the best description available to us for multi-electron atoms. This section will summarize some important quantum mechanical theories relating to the Ar atom and clarify the various quantum notations that are used in this analysis to represent the electronic states of Ar.

The Argon atom exists on Earth typically in an electronically neutral state with 18 electrons bound to the nucleus. The coulomb attraction of the individual electrons is generally toward the central nucleus, but experimental evidence indicates that the electrons do not collapse on the nucleus as the classical electromagnetic theory would predict. Instead, as predicted by quantum theory, the electrons exist in "stationary states" about the nucleus due to their wave nature coupled with the uncertainty principle. The quantum electronic state is represented mathematically as a wavefunction, Ψ , which is an eigenfunction of the time-independent Schrodinger wave equation

$$\hat{H}_e \Psi = E_e \Psi, \quad (3.1)$$

where \hat{H} is the hamiltonian operator which depends on the atom's potential energy, and E is the total electron energy eigenvalue [14]. The notations used to denote the electron states within the Ar atom are based on the wavefunctions solved for a simpler atom with a single electron, or the hydrogenlike atom. Unlike multielectron atoms, such as Ar, the wavefunction for the electron in a hydrogenlike atom can be found analytically by solving the time-independent wave equation in spherical coordinates r, θ, ϕ as

$$\left(-\frac{h^2}{8\pi^2\mu}\nabla^2 - \frac{Ze^2}{r}\right)\Psi(r, \theta, \phi) = E_e \Psi(r, \theta, \phi), \quad (3.2)$$

where e is the elementary charge, Z is the number of charges on the nucleus, and μ is the reduced mass of the atom. The above can be solved using separation of variables to give the following solution for the hydrogenlike wavefunction,

$$\Psi_{nlm}(r, \theta, \phi) = \sqrt{\left(\frac{2Z}{na_o}\right)^3 \frac{(n-l-1)!}{2n[(n+l)!]}} e^{-\frac{Zr}{na_o}} \left(\frac{2Zr}{na_o}\right)^l L_{n-l-1}^{2l+1}\left(\frac{2Zr}{na_o}\right) Y_l^m(\theta, \phi), \quad (3.3)$$

where a_o is the bohr radius, $L_{n-l-1}^{2l+1}\left(\frac{2Zr}{na_o}\right)$ are the generalized Laguerre polynomials, and $Y_l^m(\theta, \phi)$ is the spherical harmonic of degree l and order m [15]. The most traditional

notation for the quantum states of the atom includes the quantum numbers n , l , and m , which are seen in the hydrogenlike wavefunction representing the principle, the orbital, and the magnetic quantum number respectively. The spin quantum number, m_s , is the fourth quantum number needed to uniquely describe the electronic states of the hydrogenlike atom, where m_s takes the values of $\pm 1/2$ and represents the intrinsic angular momentum of the electron [16].

For a multi-electron atom, like Ar, the Shrodinger equation is

$$\left(-\frac{\hbar^2}{2m_e} \sum_{i=1}^k \nabla_i^2 - \sum_{i=1}^k \frac{Ze^2}{r_i} + \sum_{i=1}^{k-1} \sum_{j=i+1}^k \frac{e^2}{r_{ij}} \right) \Psi_{nlm}(r, \theta, \phi) = E_e \Psi_{nlm}(r, \theta, \phi). \quad (3.4)$$

This equation is not separable and thus an exact solution is not possible due to the complexity of the coulomb interaction between the electron group [17]. Still, the hydrogenlike wavefunctions represent a reasonable approximation of the available stationary states of the multielectron atom and thus the simple quantum numbers (n, l, m, m_s) associated with the hydrogenlike wavefunctions can be very useful in accounting for states of multielectron atoms, like Ar. As an additional restriction, the fermion characteristic of electrons prohibit any two electrons within a multielectron atom from occupying the same stationary state. This is expressed in the Pauli exclusion principle as the rule that no two electrons in an atom can possess the exact same set of quantum numbers, n, l, m, m_s . Thus, the most elementary notation to describe the electrons in the Ar atom is to assign each with a unique set of these four quantum numbers.

Within a multielectron atom, electrons generally fill the lowest energy states first, with the next electron filling the next lowest energy level until all the electrons are assigned sequential energy states with distinct values of n, l, m , and m_s [16]. This is known as the *aufbau* or building-up principle which leads to a representation of the ground state of an atom with Z electrons. The electron configuration of a multielectron atom denotes the distribution of the electrons among the various orbitals with quantum numbers n and l . It is common when expressing the electron configuration to denote the numerical value of l as a letter. The use of the letters $s, p, d, f...$ for the values $l = 0, 1, 2, 3...$ is convenient to avoid confusion with other numbers in the configuration. The number of electrons within each orbital is indicated with a superscript of the orbital letter in the form nl^x . A filled orbital obviously has a uniquely well defined set of electronic states, but a partially filled orbital could represent a variety of electronic states with different combinations of m and m_s . The ground state configuration of Ar is

$$1s^2 2s^2 2p^6 3s^2 3p^6$$

with each nl orbital being filled with the maximum number of electrons, which is also known as a closed shell configuration. The closed shell configuration of Ar makes it very stable and resistant to bonding with other elements.

We will be concerned in this study, not only with ground state Ar, but also electronic states of higher energy. The most common Ar excited states encountered are generated by one $3p$ electron from the ground state configuration being raised into a higher energy

orbit. In this sense, Ar is at an interesting position on the periodic table, as the simple *aufbau* principle would indicate that the next highest energy state would involve excitation to a 3d orbital. Although the 3s, 3p, and 3d orbitals of the hydrogenlike atom theoretically have the same energy, the coulomb repulsion of the other electrons in the multielectron atom will tend to raise the energy of the states with higher angular momentum. In fact the 4s orbital in Ar has a lower total energy than the 3d orbital. Thus, an Ar 3p electron excited to the next highest energy level would be in the 4s orbital and the excited state electron configuration would be

$$1s^2 2s^2 2p^6 3s^2 3p^5 4s^1.$$

The above excited configuration for Ar with a 4s outer electron is of particular interest in this study, as the metastable state discussed in the introduction exists in this configuration. Also of special interest are the configurations involving excitation of a 3p electron to the 4p or 5p orbitals, or

$$1s^2 2s^2 2p^6 3s^2 3p^5 4p^1,$$

$$1s^2 2s^2 2p^6 3s^2 3p^5 5p^1,$$

as states with these configurations will be important in the diagnostic techniques used in this study. As a shorthand notation for these excited electron configurations, only the partially filled orbitals are written and the filled core orbitals are ignored, which results in the notation $3p^5 4s^1$, $3p^5 4p^1$ and $3p^5 5p^1$ for our configurations of interest. The possible electronic states derived from these configurations will now be discussed, along with various notations that are helpful in categorizing certain spectroscopic aspects of the quantum states. An electron configuration can be divided into different energy levels by further classifying the atom based on the spin and orbital angular momentum of each electron. If the orbital angular momentum of each electron, l_i , interacts strongly with the others, then the total orbital angular momentum vector is $\mathbf{L} = \Sigma \mathbf{l}_i$, with L equaling the magnitude of \mathbf{L} . Similarly, the total spin angular momentum vector of the atom is $\mathbf{S} = \Sigma \mathbf{m}_s$, with magnitude S. This type of interaction is known as L-S or Russell-Saunders coupling. The total angular momentum vector \mathbf{J} is $\mathbf{L} + \mathbf{S}$. These three momenta vectors can be written in a notation called a term symbol, which further identifies the particular electronic state of the configuration. The term symbol has the form

$$^{2S+1}L_J$$

where L is denoted with a capital letter S, P, D, \dots in the same way as l . [16] The $2S+1$ term is called the multiplicity and determines the number of electronic states that are available for a total orbital angular momentum \mathbf{L} . For a multiplicity of three ($2S+1=3$), the spin vector can combine with \mathbf{L} in three different orientations to form three different J values. A multiplicity of one ($2S+1=1$) would only have a single value for J for each L. For the ground state of argon with the configuration of $1s^2 2s^2 2p^6 3s^2 3p^6$, the term symbol is 1S_0 , where L, S, and J are all zero.

For an excited Ar atom, as with other heavy noble gases, it is useful to consider the angular momenta coupling between the partially filled orbitals, which defines the electron states. For the excited $1s^2 2s^2 2p^6 3s^2 3p^5 4s^1$ configuration, the total orbital and spin

angular momentum of the $1s^2 2s^2 2p^6 3s^2$ inner core is zero, but the partially filled $3p^5$ and $4s$ orbitals have non-zero angular momenta that are coupled. The five electrons remaining in the core p state have an orbital angular momentum and a spin angular momentum equal and opposite to the one electron that was removed. This gives the core $3p^5$ configuration an orbital angular momentum of $L_c=1$ and a core spin of $S_c=1/2$ while the remaining electron in the $4s$ shell has $l = 0$ and $m_s = 1/2$. These can combine to form 4 possible term symbols 1P_1 , 3P_0 , 3P_1 and 3P_2 . L-S coupling provides a good model to approximate the energy states of this $3p^5 4s^1$ configuration of Ar [18].

For higher energy excited states of Ar, it is more reasonable to assume that the total angular momentum of the outer electron will couple to the total angular momentum of the non-excited electrons, referred to as the electron core. This type of coupling is called pair coupling. In pair coupling, the various combinations of the angular momenta of the core and excited electron will result in numerous states which are best sorted by the Racah notation, described below. The energy states of the $3p^5 4p^1$ and $3p^5 5p^1$ configurations can both be represented by pair coupling since the excited electron has much more energy than the electron core. This $3p^5 np^1$ configuration, where $n=4$ or 5 , will be used as an example to demonstrate Racah notation since these configurations are essential to the diagnostic experiment in this work. For the $3p^5 np^1$ configuration, the $3p^5$ core has total orbital angular momentum ($L_c=1$) and spin angular momentum ($S_c=1/2$) which combine to form the total core angular momentum $\mathbf{J}_c=\mathbf{L}_c+\mathbf{S}_c$. In this case L_c and S_c can combine in parallel or anti-parallel to give a total core angular momentum of $1/2$ or $3/2$. The orbital angular momentum of the excited electron is then coupled to \mathbf{J}_c to give an intermediate resultant angular momentum $\mathbf{K}=\mathbf{J}_c+\mathbf{l}$. For the $3p^5 np$ configuration of Ar the outer electron has $l=1$ resulting in $K=1/2$ or $3/2$ for $J_c=1/2$ and $K=1/2, 3/2$ or $5/2$ for $J_c=3/2$. The spin of the outer electron \mathbf{s} must then be added to these five possible intermediate resultant \mathbf{K} values to give a total angular momentum of the atom $\mathbf{J}=\mathbf{K}+\mathbf{s}$. Each of the five possible K terms will have two J values associated with them, since the spin of the outer electron can be coupled to K in both parallel or anti-parallel. This results in 10 possible energy states for the $3p^5 np^1$ configuration. For an atom where this type of pair coupling is prevalent the terms are most clearly represented by Racah's symbols

$$nl[K]_J$$

where nl is the orbital of the outer electron, K is the magnitude of $\mathbf{K}=\mathbf{J}_c+\mathbf{l}$, and \mathbf{J} is the total angular momentum of the atom [19]. In Racah notation a prime after the l is used if the angular and spin momenta for \mathbf{J}_c are coupled in anti-parallel and no prime is used if they are in parallel. The pair coupled energy states represented in Racah notation for the $3p^5 4s^1$, $3p^5 4p^1$, and $3p^5 5p^1$ configurations are shown in Table 1 along with the corresponding Paschen symbols which will be described next. Note that the pair coupling approximation is best suited for the higher energy $3p^5 5p^1$ and $3p^5 4p^1$ configurations but is only a rough approximation for the $3p^5 4s^1$ configuration which is represented better by L-S coupling [20].

The most common way to identify the electronic states of Ar, albeit less detailed, is with Paschen symbols, which will be the primary notation used in this work. Paschen notation was developed during an attempt to fit the spectrum of Ne to a hydrogen-like

Table 1: Energy levels

Electron Configuration	Paschen	Racah
$3p^5 4s^1$	$1s_2$	$4s' \left[\begin{smallmatrix} 1 \\ 2 \end{smallmatrix} \right]_1$
	$1s_3$	$4s' \left[\begin{smallmatrix} 1 \\ 2 \end{smallmatrix} \right]_0$
	$1s_4$	$4s \left[\begin{smallmatrix} 3 \\ 2 \end{smallmatrix} \right]_1$
	$1s_5$	$4s \left[\begin{smallmatrix} 3 \\ 2 \end{smallmatrix} \right]_2$
$3p^5 4p^1$	$2p_1$	$4p' \left[\begin{smallmatrix} 1 \\ 2 \end{smallmatrix} \right]_0$
	$2p_2$	$4p' \left[\begin{smallmatrix} 1 \\ 2 \end{smallmatrix} \right]_1$
	$2p_3$	$4p' \left[\begin{smallmatrix} 3 \\ 2 \end{smallmatrix} \right]_2$
	$2p_4$	$4p' \left[\begin{smallmatrix} 3 \\ 2 \end{smallmatrix} \right]_1$
	$2p_5$	$4p \left[\begin{smallmatrix} 1 \\ 2 \end{smallmatrix} \right]_0$
	$2p_6$	$4p \left[\begin{smallmatrix} 3 \\ 2 \end{smallmatrix} \right]_2$
	$2p_7$	$4p \left[\begin{smallmatrix} 3 \\ 2 \end{smallmatrix} \right]_1$
	$2p_8$	$4p \left[\begin{smallmatrix} 5 \\ 2 \end{smallmatrix} \right]_2$
	$2p_9$	$4p \left[\begin{smallmatrix} 5 \\ 2 \end{smallmatrix} \right]_3$
	$2p_{10}$	$4p \left[\begin{smallmatrix} 1 \\ 2 \end{smallmatrix} \right]_1$
$3p^5 5p^1$	$3p_1$	$5p' \left[\begin{smallmatrix} 1 \\ 2 \end{smallmatrix} \right]_0$
	$3p_2$	$5p' \left[\begin{smallmatrix} 1 \\ 2 \end{smallmatrix} \right]_1$
	$3p_3$	$5p' \left[\begin{smallmatrix} 3 \\ 2 \end{smallmatrix} \right]_2$
	$3p_4$	$5p' \left[\begin{smallmatrix} 3 \\ 2 \end{smallmatrix} \right]_1$
	$3p_5$	$5p \left[\begin{smallmatrix} 1 \\ 2 \end{smallmatrix} \right]_0$
	$3p_6$	$5p \left[\begin{smallmatrix} 3 \\ 2 \end{smallmatrix} \right]_2$
	$3p_7$	$5p \left[\begin{smallmatrix} 3 \\ 2 \end{smallmatrix} \right]_1$
	$3p_8$	$5p \left[\begin{smallmatrix} 5 \\ 2 \end{smallmatrix} \right]_2$
	$3p_9$	$5p \left[\begin{smallmatrix} 5 \\ 2 \end{smallmatrix} \right]_3$
	$3p_{10}$	$5p \left[\begin{smallmatrix} 1 \\ 2 \end{smallmatrix} \right]_1$

theory before the full development of quantum theory, but the simple notation remained popular and is still common today. For example, for the $3p^5 4s^1$ configuration, the lowest energy term of 3P_2 has the Paschen symbol of $1s_5$. The Paschen symbols are numbers and letters roughly representing the energy and orbital angular momentum of each state, but the numbering scheme begins with the first excited state as opposed to representing the principal quantum. The letter can take values of s, p, and d like those of orbital angular momentum, although it can not always be concluded that these correspond to $l=1,2,3$ and so on. The subscript represents a numerical accounting of the states in order of decreasing energy, but this too is only approximate. A summary of the Racah and Paschen symbols for the $3p^5 4s^1$, $3p^5 4p^1$ and $3p^5 5p^1$ configurations is in table 1. From this point forward, Paschen notation will be used exclusively to identify atomic energy states, unless another notation is absolutely necessary to clarify a specific aspect of that state.

3.2 Radiative Transitions in Argon

The theory of radiative transitions have a fundamental role in the Ar plasma diagnostics performed in this work. Transitions between energy states can be caused by absorption by an atom of energy as electromagnetic radiation. The energy exchanged between the absorbed photon and the atom is given by Bohr's frequency relation,

$$h\nu_{nm} = E_n - E_m, \quad (3.5)$$

where E_n and E_m are the energies of the upper state n and the lower state m respectively, h is Planck's constant and ν_{nm} is the frequency of the radiation corresponding to the transition between states n and m . A theoretical treatment of the radiative transition must begin with the interaction of the electric field of the radiation with the total electron charge distribution within the atom. To a first order approximation, the influence of an electromagnetic wave on an atomic system is the interaction of the radiative electric field with the electric dipole moment M of the atom. For the case of the electric field of the radiation in the x direction, the interacting electric dipole moment component is

$$M_x = \sum e_k x_k, \quad (3.6)$$

where e_k are the electron charges of coordinates x_k . By introducing the energy of interaction between the radiation field and dipole moment into the Schrodinger wave equation, it can be shown that the probability of the transition between the states is proportional to the transition dipole moment R^{mn} [16]. The component of this transition dipole moment is

$$R_x^{mn} = \int \Psi_m^* M_x \Psi_n dx dy dz, \quad (3.7)$$

where Ψ_m and Ψ_n are the wave functions of the two states. If R^{mn} is non-zero then there will be some probability of absorption between the two states and such a transition is termed "allowed". If R^{mn} is zero, then the transition is considered "forbidden" and will not occur as a dipole transition. In the case of the hydrogenlike atom, the component of R^{mn} can be solved exactly by

$$R_x^{mn} \propto \int \Psi_m^* x \Psi_n dx dy dz. \quad (3.8)$$

Examining the above solutions reveal that most all R^{mn} of the hydrogenlike atom become zero, unless specific changes in the quantum numbers between both states occur. The specific nonzero R^{mn} cases are identified by "selection rules" which indicate the allowed transitions. A primary selection rule determined from the above solutions is that the difference in the quantum number l between the two states must be

$$\Delta l = \pm 1.$$

For a multielectron atom like Ar, the coupling of orbital and spin angular momentum lead to the rigorous dipole moment selection rule

$$\Delta J = 0, \pm 1, J = 0 \nrightarrow J = 0$$

where the restriction $J = 0 \nrightarrow J = 0$ indicates that a transition between a state with $J = 0$ to another state with $J = 0$ is forbidden. If L-S coupling is a good approximation, then the following are approximate selection rules

$$\Delta L = 0, \pm 1$$

$$\Delta S = 0.$$

The above discussion concerning the transition dipole moment assumed a first order approximation for the incident electromagnetic wave. Higher order approximations would induce additional energies of interaction of the radiation other than with the electric dipole and allow different transitions to occur. These higher order interactions, including magnetic dipole and electric quadrupole interaction, result in interaction energies that are generally much less than those of the electric dipole interaction and thus the probability of absorption is often orders of magnitude lower [16].

A typical mode of decay for an electronically excited atom from state n to state m is to emit a photon of radiation with an energy $h\nu_{nm}$ equal to the decay transition energy, $E_n - E_m$. It can be shown that the probability of this spontaneous emission is proportional to the corresponding transition dipole moment R^{nm} for the given states discussed above. Therefore, excited Ar states will exhibit spontaneous emission in accordance with the same select rules as derived above for absorption.

The intensity of the emission, I_{em} , which is the radiation energy density emitted per second from excited Argon atoms with a concentration N is given by

$$I_{em}^{nm} = Nh\nu_{nm}A_{nm} \quad (3.9)$$

where A_{nm} is the Einstein probability of spontaneous emission and has units of s^{-1} [16]. In the case of dipole radiation, A_{nm} is related to the transition dipole moment as

$$A_{nm} = \frac{64\pi^4\nu_{nm}^3}{(4\pi\epsilon_0)3hc^3}|R^{nm}|^2. \quad (3.10)$$

The decay time of an excited state n of an atom is related to the Einstein coefficient A_{nm} by the equation

$$-\frac{dN}{dt} = \sum_m A_{nm}N \quad (3.11)$$

where the sum over m represents all of the possible transitions for n . This equation leads to the expression for the radiative lifetime, τ , of the excited state n .

$$\tau = \frac{1}{\sum_m A_{nm}} \quad (3.12)$$

For allowed electric dipole transitions, τ is on the order of 10^{-8} s. States that are not coupled to any lower state with an allowed electric dipole transition may have a weaker coupling through a higher order electromagnetic coupling which results in a much longer lifetime. The radiative lifetime may be on the order of 10^{-3} s for magnetic dipole

transitions and on the order of seconds for quadrupole transitions. The comparatively long τ of these excited states produce a relatively stable radiative lifetime characteristics and thus these states are termed “metastable” [16].

The dipole transitions from the lowest Ar excited $1s$ states, which include two Ar metastable states of interest, to the ground state will now be considered. The four possible Ar $1s$ states, $1s_5$, $1s_4$, $1s_3$, and $1s_2$, have J values derived earlier as, $J=2$, 1 , 0 and 1 respectively, whereas the Ar ground state has $J=0$. Direct application of the ΔJ selection rules leads to allowed transitions from the $1s_4$ and $1s_2$ to the ground state since $\Delta J=1$, but the transition from $1s_5$ to the ground state is forbidden since $\Delta J=2$ is not allowed and likewise the transition from $1s_3$ to the ground state is forbidden since $J=0 \nrightarrow J=0$. The forbidden nature of the two latter dipole moment transitions to the ground state reveals the metastable characteristic of the $1s_5$ and $1s_3$ states. Correspondingly, the radiative lifetime of the $1s_5$ and $1s_3$ metastable states have been calculated to be very long, with a τ of 56 s and 45 s respectively [21]. These can be compared to the radiative lifetimes of the $1s_4$ and $1s_2$ states which were determined semi-empirically to be 9 orders of magnitude shorter at 10 ns and 3 ns respectively [8].

The longer radiative lifetime of a metastable state generally results in a slower rate of decay of the state in a kinetic analysis. Therefore, if various excited states of an atom in a gas discharge are being populated uniformly by direct excitation from the ground state or by cascading from higher excited states, the concentration of a metastable state will tend to grow to greater proportions due to its slow decay rate. As a result, metastable concentrations are generally very high, such as those for the $1s_5$ and $1s_3$ states in a sustained Ar discharge. Since these Ar metastable states also lie at fairly high energies above the ground state (11.5 eV), their large concentration indicates that significant internal energy may be contained and stored in the metastable population and could be a considerable factor in kinetic and energy transfer processes.

The $3p \rightarrow 1s$ and $2p \rightarrow 1s$ transitions in Ar both include transitions into the $1s$ metastable states and are important in this work. These transitions are allowed since l changes from $l=1$ in the $3p$ and $2p$ configuration to $l=0$ in the $1s$ configuration. Some of these $3p \rightarrow 1s$ and $2p \rightarrow 1s$ transitions will terminate on the $1s_2$ and $1s_4$ levels, resulting in rapid decay to the ground state, while others will decay into the longer lived $1s_3$ and $1s_5$ metastable states. Two specific transitions that were of great interest in this work were $3p_9 \rightarrow 1s_5$ and $3p_5 \rightarrow 1s_4$ causing emission at wavelengths of 420.07 nm and 419.83 nm respectively. Comparison of the optical emission from these two transitions represented a convenient method to analyze the electron impact excitation contributions from the Ar ground and metastable states, as is described further in the following sections.

3.3 Electron Impact Cross Sections

An important mechanism for atoms to be excited to higher energy states, besides the absorption of radiation discussed above, is through direct electron impact. In a gas

discharge, where the ionized gas contains free electrons that are accelerated to high kinetic energies in the presence of an electric field, electron impact is the primary source of excitation and ionization. The electron impact cross section for a particular excitation is a hypothetical area around a target atom that represents a surface, where if an electron of energy ϵ crosses that surface then that excitation will occur. The electron impact cross section, usually expressed in cm^2 , is proportional to the probability of exciting an atom by electron impact into a higher energy level. Once excited into a higher state, the atom will generally decay to a lower state by a radiative transition. Detection of this radiation is a common method to determine the rate of electron impact excitation and thus the electron impact cross section. This method is complicated by the fact that the excited state may decay by radiation to several different lower states. Another complication is that the excited state can be populated not only by direct electron impact, but also by cascading radiative transitions from even higher states. The electron impact cross section determined from measuring the intensity of a single radiative transition from the higher state is termed the *optical cross section* and is the sum of the direct cross section and cascade contributions from all higher levels for a specific electron energy ϵ [22].

For the Ar optical emission diagnostics in this work, the optical cross section is ideal for relating emission intensities to the density of the initial states. The optical cross section for an Ar atom initially in the ground state and excited through electron impact of energy ϵ is given as $\sigma_{nm}(\epsilon)$ where n is the excited higher state and m is the lower state where the radiation transition terminates, but is not necessarily the initial state. This direct electron impact excitation from the ground state in this work will be termed “direct excitation”. These cross sections can also describe excitation to an ionized upper state n which radiates to a lower ionized state m . Electron impact excitation from the Ar $1s_3$ and $1s_5$ metastable states is also important for the diagnostics in this work and will be termed “step-wise excitation”. The notation for the optical cross section for an Ar atom initially in the metastable state is $\sigma_{nm}^*(\epsilon)$, where it is noted that m again is the termination state of the radiative transition, but may or may not be initial state of excitation. A comprehensive set of experimental measurements of $\sigma_{nm}(\epsilon)$ and $\sigma_{nm}^*(\epsilon)$ for Ar have been compiled by Lin et al. ([11],[20],[23]) which are used extensively herein to study the determination of Ar state densities from optical emission data.

3.4 Electron Energy Distribution Function

Free electrons in a gas discharge have a wide range of energies. In a gas discharge, the applied electric field accelerates electrons which gives them increased energy until they collide with another particle and exchange energy. Some electrons may travel further, and therefore increase their energy, before a collision takes place which creates a distribution of electron energies within a gas discharge [24]. This distribution of energies can be calculated by considering a constant applied electric field, the density of background atoms/molecules, the energy dependent cross sections for collisions between electrons and background targets, and the amount of energy transferred during the various collisional excitations of the background atoms/molecules. The general equation for the motion of

a group of particles is given by the Boltzmann equation, which for electrons in a gas discharge is

$$\frac{\partial f(v)}{\partial t} + v \cdot f(v) - \frac{e}{m} E \cdot \Delta_v f(v) = C[f(v)] \quad (3.13)$$

where $f(v)$ is the electron velocity distribution, $-eE/m_e$ is the force on the electrons applied by the electric field E , v are the velocity coordinates, Δ_v is the velocity gradient operator and $C[f(v)]$ represents the changes on the distribution caused by collisions [25]. The computational package BolSig is a program that solves the Boltzmann equation for a set of user inputs and was used in this work to calculate the electron energy distribution function, $f(\epsilon)$, or the EEDF [26]. The user inputs an E/N value, where N is the density of the background gas, along with a composition of gases in the discharge. BolSig uses a built-in set of collisional cross sections to calculate the $C[f(\epsilon)]$ contribution for a variety of gases, but also allows the user to add cross sections if needed. BolSig can only produce solutions of the EEDF for steady state cases where the electric field and electron distribution is approximately stationary in time. For Ar gas discharges at 5 mTorr, the EEDFs were calculated with BolSig and were essential to the analyses in this work, especially when calculating the effects of the energy dependent excitation cross sections. If the applied electric field is extremely transient (i.e. 1000's of volts per μ s) in time the electron energies may not reach the distribution given by $f(\epsilon)$ solved from equation 3.13. Such is the case in this work during the Ar discharge breakdown period where the highly transient electric field caused a high uncertainty in the EEDF used to simulate the spectral lines of the optical emission.

3.5 Optical Emission Intensity

The optical emission intensity, I_{em}^{nm} , defined earlier in terms of the density of the emitting state, can now be defined in terms of the kinetic and electrical properties of a gas discharge. The optical cross section and EEDF data for Ar can be combined with information on the densities of the target states in the discharge to calculate the relative emission intensity for a particular set of transitions. These theoretical emission intensities can then be compared to experimental optical emission measurements. The emission intensity for a single transition excited from target atoms initially in the ground state is given by

$$I_{em}^{nm} = \frac{hc}{\lambda_{nm}} N N_e \left(\frac{2e}{m_e} \right)^{1/2} \int_0^\infty \sigma_{nm}(\epsilon) \epsilon f(\epsilon) d\epsilon \quad (3.14)$$

where N is the number density of ground state atoms and N_e is the number density of electrons [25]. In addition to optical emission due to direct excitation from the ground state, step-wise electron excitation from a metastable state may cause non-negligible contributions to the optical emission. The total density of Ar atoms in a metastable state can be given as N^* which is the sum of the densities in the $1s_5$ and $1s_3$ metastable states. A statistical weighting factor, g_i , was used to give the specific density of either the $1s_5$ or $1s_3$ state as $g_i N^*$. Based on previous theoretical and experimental work, which predicted a statistical weight ratio of 5 : 1 for the $1s_5$ or $1s_3$ states, statistical weighting

factors were assigned to be $g_{1s5}=5/6$ and $g_{1s3}=1/6$ [20]. Each step-wise excitation cross section, $\sigma_{nm}^*(\epsilon)$, corresponded to excitation from either the $1s_5$ or $1s_3$ metastable state and thereby was associated with its respective g_i value in calculating the simulated emission intensity. Combining contributions of excitation from both metastable and ground state atoms for a single transition gives

$$I_{em}^{nm} = \frac{hc}{\lambda_{nm}} N N_e \left(\frac{2e}{m_e} \right)^{1/2} \int_0^\infty [N \sigma_{nm}(\epsilon) + g_i N^* \sigma_{nm}^*(\epsilon)] \epsilon f(\epsilon) d\epsilon. \quad (3.15)$$

Step-wise excitation begins to noticeably contribute to the optical emission spectrum if the product of the metastable state density and optical cross section, $g_i N^* \sigma_{nm}^*(\epsilon)$, is on the same order as $N \sigma_{nm}(\epsilon)$.

For Ar, the optical cross sections from the metastable states, $\sigma_{nm}^*(\epsilon)$, can be much larger than those from the ground state, $\sigma_{nm}(\epsilon)$, but this is countered by N^* being much less than N [11, 20]. In typical experiments, some contribution to I_{em}^{nm} from step-wise excitation can be observed in an Ar gas discharge.

A simulated spectrum of emission line intensities, $I_{em}(\lambda)$, can be generated by considering all transitions in a spectral region by the equation

$$I_{em}(\lambda) = \sum_{n,m} I_{em}^{nm} \delta(\lambda_{nm}) \quad (3.16)$$

where λ is the emission wavelength and $\delta(\lambda_{nm})$ is the dirac delta function at the resonant wavelength for the transition between states n and m . For the calculations relating to the optical emission diagnostic in this work, a simulation of the relative intensities of $I_{em}(\lambda)$ is sufficient for the desired analysis of step-wise excitation from metastable Ar. Parameters that are constant for all I_{em}^{nm} cancel in an analysis of relative emission intensities, which includes the total electron density value, N_e . Therefore the simulated spectrum of relative emission line intensities can be determined by

$$I_{em}(\lambda)_{relative} = \sum_{n,m} \frac{\delta(\lambda_{nm})}{\lambda_{nm}} \int_0^\infty \left[\sigma_{nm}(\epsilon) + g_i \frac{N^*}{N} \sigma_{nm}^*(\epsilon) \right] \epsilon f(\epsilon) d\epsilon, \quad (3.17)$$

where it is clear that $I_{em}(\lambda)_{relative}$ is a strong function of the ratio of Ar metastable to ground state number densities, N^*/N , and the EEDF.

3.6 Diode Laser Absorption Spectroscopy

Diode laser absorption was used to verify the calculations and assumptions in this work of Ar metastable densities based on optical emission measurements. The following is a detailed derivation of how the absolute Ar metastable density was calculated using known spectroscopic constants of Ar along with an experimental absorption spectrum. Laser absorption spectroscopy is a technique often used to measure the density of a light absorbing material [27, 13]. A beam of light with initial intensity I_o is passed through a

material. The light that exits the material has a reduced intensity I . When the material is an atomic gas, such as Ar in this work, the absorbed light will cause the atoms to transition to higher energy levels following the selection rules previously discussed in section 3.2. The amount of light lost by absorption is related to the initial intensity of the light and is given by the following equation,

$$I - I_o = -\Delta I = I_o \alpha \Delta l \quad (3.18)$$

where α is the absorptivity of the gas and Δl is a section of length of the absorbing gas. By assuming Δl is very small, ΔI can be replaced with the differential dI . In this situation, the gas absorbs a small amount of light and ΔI is replaced with dI . The resulting equation is

$$\frac{dI}{I_o} = -\alpha dl \quad (3.19)$$

and the equation can be solved by integrating over the total length of the gas, l , and over the two levels of light intensity,

$$\int_{I_o}^I \frac{dI}{I_o} = -\alpha \int_0^l dl. \quad (3.20)$$

The absorptivity α can be further defined by

$$\alpha = N_i^* \sigma_{abs}(\nu) \quad (3.21)$$

where N_i^* is the number density of absorbing atoms, either in the $1s_5$ or $1s_3$ Ar metastable state, and $\sigma_{abs}(\nu)$ is the absorption cross section of the atom [28]. This cross section represents the likelihood for an atom to absorb a photon of frequency ν .

The absorptivity, α , as written is independent of l , which means that N^* within the length l of gas is assumed to be uniform. The transmission ratio, I/I_o , can now be expressed as

$$\frac{I}{I_o} = \exp[-N_i^* l \sigma_{abs}(\nu)]. \quad (3.22)$$

The absorption cross section is dependent on the incident photon frequency as well as the properties of a particular radiative transition and can be written as

$$\sigma_{abs}(\nu) = h\nu \frac{B_{mn}}{c} g(\nu) \quad (3.23)$$

where B_{mn} is the Einstein transition probability of absorption, also known as the Einstein B coefficient, and $g(\nu)$ is the observed line shape function [28]. The Einstein coefficient B_{mn} is representative of the probability for an atom to absorb a photon of frequency ν_{nm} and transition from state m to state n. The Einstein B coefficient is related to the Einstein A coefficient by

$$B_{mn} = \frac{c^3}{8\pi h \nu_{nm}^3} A_{nm}. \quad (3.24)$$

The primary frequency dependence of the absorption is represented by the line shape function $g(\nu)$. For an atomic gas the laser diode absorption spectrum is typically comprised of narrow absorption peaks, or lines, at resonant frequencies, each representing a

radiative transition. An experimentally observed spectral line is always broadened due to various effects including natural, Doppler, and pressure broadening. Natural broadening is always present due to the quantum uncertainty principle and is related to the radiative lifetime of the states but is often negligible compared to Doppler and pressure broadening. For this work, Ar is studied at a relatively low pressure, so both natural broadening and pressure broadening from collisions are negligible compared to thermal induced Doppler broadening. For Doppler broadening the line shape function is a gaussian function given by

$$g(\nu) = \left(\frac{4\ln 2}{\pi \Delta\nu_d^2} \right)^{\frac{1}{2}} \exp \left[-(4\ln 2) \left(\frac{\nu - \nu_o}{\Delta\nu_d} \right)^2 \right] \quad (3.25)$$

where ν_o is the resonant frequency of the transition and $\Delta\nu_d$ is the full-width at half-max (FWHM) or Doppler width. The function is normalized to 1 when integrated over all frequencies. The doppler width is given by

$$\Delta\nu_d = \sqrt{\frac{8kT\ln(2)}{m_a c^2}} \quad (3.26)$$

where k is the Boltzmann constant, T is the gas temperature, and m_a is the mass of the individual gas atom [29]. The transmission ratio I/I_o can be represented in terms of $g(\nu)$ by combining equations 3.22 and 3.23 to obtain

$$\ln \left(\frac{I_o}{I} \right) = \frac{N_i^* l h \nu B_{mn}}{c} g(\nu). \quad (3.27)$$

In this work, the transmission coefficient is recorded over a range of discrete laser frequencies which encompasses two Ar metastable transitions. With this experimental absorption spectrum, the temperature of the absorption medium can be calculated from the shape of the absorption lines and the absolute metastable density can be calculated from the peak absorption ratio. The temperature is determined through a calculation of $\Delta\nu_d$, which is found by fitting the relative shape of the measured $\ln(I_o/I)$ to $\nu g(\nu)$, where for a diode laser frequency on the order of 40,000 GHz and a doppler width of approximately 1 GHz, $\nu g(\nu)$ is roughly a gaussian fit function. The temperature of the Ar gas discharge used in this diagnostic work is assumed to be near room temperature, although no other experimental method was used to check the temperature besides the line shape calculation. To calculate the total absolute metastable density, N^* , the $1s_5$ or $1s_3$ density, N_i^* , is replaced with the weighted parameter $g_i N^*$ and equation 3.27 is solved for N^* . In this calculation, only the peak absorption value of the experimental spectrum at the resonant frequency (i.e. the smallest transmission ratio I_{peak}/I_o) is required. The simplified equation solving for a value of uniform total metastable density N^* across the gas length, l , is

$$N^* = \ln \left(\frac{I_o}{I_{peak}} \right) \frac{c \Delta\nu_d \sqrt{\pi}}{g_i l h \nu_o B_{12} 2\sqrt{\ln 2}}. \quad (3.28)$$

The assumption was made earlier that the density of Ar metastable absorbing N^* was uniform throughout the gas length l . Equation 3.28 can also be re-written to solve for the column density,

$$N^*l = \ln \left(\frac{I_o}{I_{peak}} \right) \frac{c \Delta\nu_d \sqrt{\pi}}{g_i h\nu_o B_{12} 2\sqrt{\ln 2}}. \quad (3.29)$$

which can be calculated without assumptions regarding the absorption length and uniformity in metastable density. In this work in section 5.2, the column density measurement was used through different vertical positions in the discharge tube with various gas lengths to help determine the actual radial uniformity of the metastable density and assign an effective constant gas length parameter, l .

CHAPTER 4

Previous Work

4.1 Argon Metastable Density Measurements

4.1.1 Optical Emission Spectroscopy

Optical emission spectroscopy (OES) provides a non intrusive way to determine different parameters of a plasma by studying the light emitted from the discharge. OES is a widely used technique because the emitted light can be studied without affecting the discharge. Plasma parameters such as electron temperature, gas temperature, and metastable densities can be measured through the application of OES [30]. Significant work has been done previously to calculate temperatures and densities of species in an Ar discharge using OES. For many years, the electron temperature could be measured within an Ar plasma by OES through spectral line intensity ratios [31]. Recently, the electron density has been measured by combining OES measurements with kinetic modeling which considers collisional processes within the discharge [32]. Schulze et al. [33] has previously calculated the Ar metastable density within a low pressure inductively coupled plasma using the theoretical branching ratios involving 5 infrared emission lines resulting from the set of $2p \rightarrow 1s$ transitions. This method relied on radiation trapping to produce differences between the experimental line intensity ratios and the theoretical branching ratios due to the relatively high density metastable states and reveal the density of the metastables. The electron energy distribution and electron impact data were not considered in these measurements, but rather the absolute metastable densities were validated by comparing their emission line ratios "a posteriori" to previously published work [33]. Most recently, the technique of Shulze et al. to measure Ar metastable densities along with a similar OES method using a more comprehensive set of emission lines was compared directly to a standard white light absorption technique [34]. Boffard et al. provided a topical review discussing how OES combined with the experimental electron impact cross section data along with the electron energy distribution function can provide a non-intrusive means to study important plasma parameters [22]. This paper emphasized the role of excitation from the metastable states in maintaining ionization in an Ar discharge. More specifically, an OES study within a pulsed Ar radio frequency inductively coupled plasma discharge displayed specific line intensity affects due to step-wise excitation from metastables [35]. This OES study showed that an emission maximum in the afterglow of the discharge was due to step-wise excitation and not just recombination. Boffard et al. specifically predicted ratios of the 420.1 nm to the 419.8 nm emission lines, which are uniquely affected by direct and step-wise excitation, to be approximately 1 : 1 during an Ar discharge with significant direct excitation and approximately 4 : 1 when emission is completely dominated by step-wise excitation out of the metastable level, such as in an Ar afterglow [36]. DeJoseph et al. experimentally determined the 420.1 nm to 419.8 nm ratio to be relatively constant in an Ar afterglow at 3.8 : 1 [35].

4.1.2 Laser Absorption

At present, the most accurate method to determine Ar metastable densities is through laser absorption spectroscopy, although this technique can be expensive and impractical outside of a laboratory environment. Hebner in 1996 performed an extensive analysis of an inductively coupled Ar plasma including a measurement of excited state densities through laser absorption spectroscopy [27]. Hebner used the best available tunable infrared laser absorption source at that time, which was an Ar-ion-laser-pumped ring titanium-sapphire laser to produce absorption spectra over a variety of Ar transitions, including $1s_5 \rightarrow 2p_8$ at 801.4 nm, $1s_4 \rightarrow 2p_7$ at 810.4 nm, $1s_3 \rightarrow 2p_4$ at 794.8 nm, and $1s_2 \rightarrow 2p_2$ at 826.6 nm. Argon excited state temperature and line integrated density were derived from these laser absorption measurements. For more than a decade, the rapid development of high performance, low-cost tunable diode lasers have allowed researchers to readily apply them to experiments in laser absorption spectroscopy. For example, tunable infrared diode lasers have been used to measure Ar metastable state densities in various applications including argon-mercury lamp development [12], element-selective gas chromatography [37] and hydrocarbon-containing Ar dusty plasmas [38]. The experimental apparatus at WPAFB used in the work herein and described in section 5.2 has been used in previous studies of dielectric barrier discharges in Ar and N_2/Ar . Williamson et al. used the WPAFB laser diode system centered at 772.4 nm to excite the $1s_3 \rightarrow 2p_2$ Ar transition and determine the population density of the $1s_3$ Ar metastable in a short pulsed dielectric barrier discharge in 100 Torr of N_2/Ar [13]. Leiweke et al. examined varying pulse durations of the N_2/Ar dielectric barrier discharge and demonstrated a gas temperature measurement [39] as well as an absolute Ar metastable density measurement [40] using the same WPAFB laser diode system.

4.2 Argon Electron Impact Cross Sections

Some of the primary calculations in this work incorporate published experimental data on electron-impact excitation cross section measurements on argon gas atoms. The following review is not a complete list of work done in the field (see review articles [41, 42]), but it does provide a standard of what values are available. The cross sections include measurements for excitation of the ground state of the atom, metastable states, and the ground state of the ion. A detailed discussion of electron-impact excitation theory and the corresponding cross sections is provided in section 3.3.

Electron-impact excitation from the Ar ground state to the $2p$ state (Paschen notation) involves excitation cross sections that have been found to be relatively large ($\sim 10^{-17}$ - 10^{-18} cm²) with short lifetimes (22-39 ns) [43, 44, 45]. The optical emissions from the $2p \rightarrow 1s$ transition that is indicative of electron-impact excitation to the $2p$ state lie in the 700-1150 nm wavelength range and are the most intense lines of the argon spectra in the visible/near-IR. The population of these levels in plasmas is determined by electron-impact excitation and radiative decay due to their large cross sections and short lifetimes. However, due to the large cascade contribution to the apparent cross

section for these levels, there is some degree of pressure dependence, which complicates their use in plasma diagnostics. In fact, variation in published apparent cross sections for these levels is seen due to the varying pressures used in the experiments. As will be discussed below, the $2p$ levels can also be readily populated through the excitation of metastable atoms.

The primary set of excitation data from the ground state used in the present work were not to the $2p$ state, but rather to the $3p$ state. This electron-impact excitation to the $3p$ state results in the next largest set of cross sections and generates optical emission from $3p \rightarrow 1s$ in the 395-470 nm spectrum range [45, 46]. This spectral range also overlaps with the wavelength range of many prominent ion emission lines, allowing easy cross calibration of atomic and ionic emissions. Compared with the $2p$ levels, however, the $3p$ levels have smaller excitation cross sections (approximately one third smaller) and longer lifetimes (75-170 ns) [11]. On the plus side, however, the cascade contribution to the $3p$ levels is generally less than that to the $2p$ levels.

Cross sections have also been measured for the excitation out of the $1s_3$ ($J = 0$) and $1s_5$ ($J = 2$) metastable levels of Ar [23, 47]. These cross sections are generally much larger (10^{-15} - 10^{-16} cm²) than the corresponding cross sections out of the ground state, although the $1s$ metastable target density is generally much lower than the ground state density. Since the two metastable levels are pure triplet levels (3P_0 and 3P_2), the pattern for excitation from the metastable levels into the ten levels of the $2p$ state is quite different from that of the 1S_0 ground state [22]. For example, the largest excitation cross sections from the metastable levels are for excitations into the $2p_4$ and $2p_9$ levels, with small cross sections for excitation into the $2p_1$ and $2p_5$ levels.

The metastable excitation cross sections into the levels of the $2p$ state are much larger than the cross sections into any other state [48]. Measurements for selected levels of the $3p$ state do indicate that the cross sections into these levels from the metastable states are much smaller. As a result, excitation of metastable atoms plays a diminished role in the population of these levels. For example, comparing ground state apparent cross sections, the value for the $3p_9$ level is 20% of the $2p_9$ cross section; whereas for metastable excitation, the $1s_5 \rightarrow 3p_9$ cross section is only about 4% of the $1s_5 \rightarrow 2p_9$ value.

In addition to the experimental measurements of the electron-impact excitation cross sections, there has also been previous publications of calculations of excitation cross sections from the argon metastable states. Srivastava et al [49] used the relativistic distorted-wave approximation to calculate the excitation of the lowest metastable states of argon (the $1s$ $J = 0, 2$ levels) to the ten higher-lying fine-structure levels of the $2p$ configuration. In later research cross section calculations were performed for excitation from the lowest $1s$ metastable states to the higher level $3p$ configuration using the same relativistic distorted-wave approximation [50].

Finally, extensive measurements have been made for the simultaneous ionization and excitation of ground state argon into the levels of the $3p^4 4p$ configuration of Ar⁺ [51, 52, 53, 54, 55, 56, 57]. Limited measurements have also been taken for selected transitions

from levels of the $3p^44d$ [54, 55] and $3p^45s$ [52] configurations. The optical emission cross sections at 50 eV for many of the $3p^44p \rightarrow 3p^44s$ transitions (420-490 nm) are larger than all but the $2p \rightarrow 1s$ transition array. However, it should be noted that 50 eV is near the peak of the cross sections for these Ar^+ levels which start at ~ 35 eV, whereas the $3p^55p$ levels start at 14.5 eV and peak at ~ 25 eV.

Excitation from the ground state of Ar^+ requires much lower energy electrons (~ 19 eV). Cross sections for excitation of ions are more limited than the cross sections available for simultaneous excitation/ionization. Using an Ar^+ ion beam as a target, Zapesochnyi et al [58, 59] have found that the peak excitation cross sections into the $3p^44p$ levels are 5-30 times larger out of the ion ground state than out of the atomic ground state. Further work in this area is necessary in light of the importance of this excitation channel in plasmas with modest ionization fractions.

CHAPTER 5

Experimental

5.1 Pulsed DC Discharge

For this study, a direct current (dc) pulsed discharge was used to generate the Ar plasma. The motivation for using the pulsed discharge was to create an environment with variable Ar metastable density, where the optical emission spectra could be easily and accurately analyzed as a function of metastable density. Figure 5.1 is a graphical representation of a dc voltage pulse (solid line) in time producing an Ar discharge along with the corresponding metastable density (dashed line) evolving in time. At the initiation of the pulse discharge, corresponding at time (i) in Figure 5.1, the Ar metastable density should be negligible assuming a flowing system with a sufficient delay between pulses to allow metastables from the previous pulse to evacuate or decay. The metastable density was also expected to be very low in the first few μs of the pulsed discharge, but then should build over time during the discharge through direct excitation, cascading from higher energy states, and a long radiative lifetime. This larger metastable density should be seen at time (ii) during the discharge, while immediately after the discharge, at time (iii) in Figure 5.1, the density should remain constant because of the long lifetime of the metastable. By collecting the optical emission spectra within small gated time periods, the resulting spectra was representative of the metastable density during each respective period. For example, emission spectra from very early in the pulse would be expected to show less evidence of step-wise electron impact excitation originating from the Ar metastable states compared to later times.

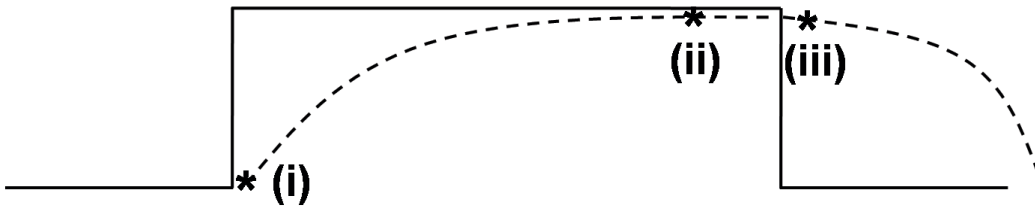


Figure 2: Pulsed discharge voltage (solid line) and metastable density (dashed line)

5.1.1 Discharge Tube and Vacuum System

The pulsed discharge tube was made of quartz, 5 cm diameter and 1 meter in length, with hollow aluminum electrodes and generated a flowing Ar discharge at 5 mTorr. The 5

mTorr discharge pressure matched the target Ar pressure for the published optical cross section data ([11],[20],[23]), so these optical cross sections could be applied without pressure correction to model the discharge spectral intensity distributions. The relatively long 1 meter tube length was used for the 5 mTorr discharge to match the pressure-distance (pd) product corresponding to the minimum breakdown voltage in the Ar Paschen curve. Several small metal probes extended through the quartz wall and were positioned to measure the plasma voltage at different lengths along the discharge tube. A sketch of the discharge chamber and its components are shown in Figure 3. The outlet of the quartz

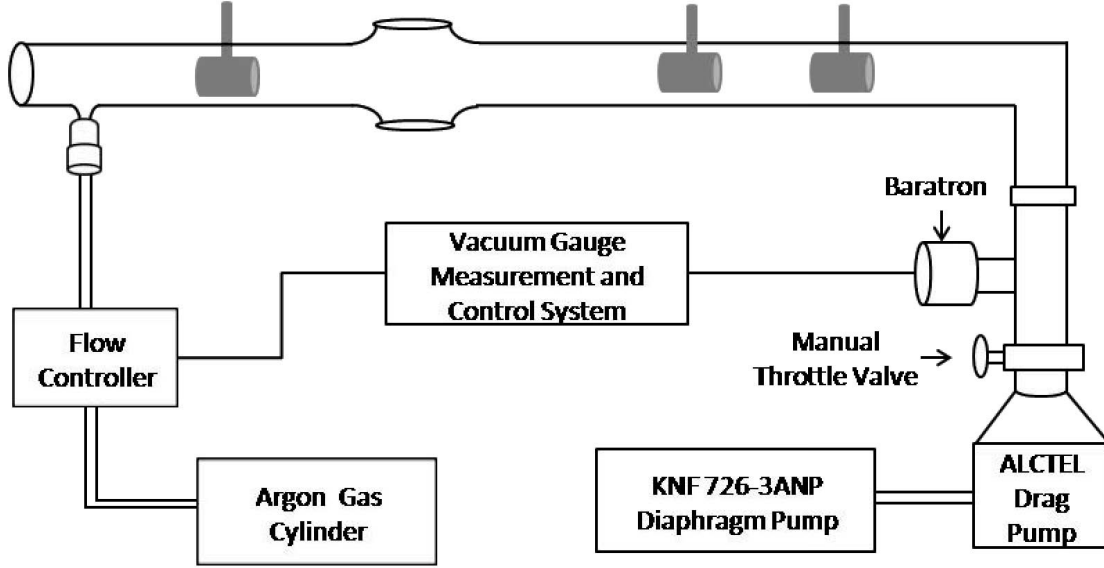


Figure 3: Discharge tube and vacuum components configuration

discharge tube was a 3.8 cm diameter quartz section that extended at a right angle from the anode end of the tube for about 12 cm. This quartz outlet section was transitioned into a metal Klein Flange which was connected to a series of 3.8 cm pipes and conflat flanges and led to a manual throttle valve, pressure transducer and the pumping system. The pumping station consisted of an ALCTEL model 5010 molecular drag pump as the primary pump and a KNF 726-3ANP diaphragm pump as the roughing pump. Electrically insulating glass wool was securely lodged within the 3.8 cm quartz outlet tube to prevent a discharge occurring between the high voltage electrode and the grounded metal vacuum flanges.

5.1.2 Power Supply

The pulsed power supply to energize the discharge was connected in series with an ohmite L225J high power 150 Ω resistor and the hollow electrode anode. A stainless steel ultra-torr fitting served as the grounded cathode of the discharge, which coupled the 6 mm inlet of the quartz tube to the plastic Ar flow tube and is shown in Figure 4. The power

supply delivered a series of dc voltage pulses, initially at 4 kV, to the anode at a rate of 10 Hz and a duration of 80 μ s each. The application of 4 kV to the anode led to electrical breakdown, usually within a few μ s, and an increase in the discharge current. The power supply was current limited and would self-regulate the applied voltage, which would typically drop from 4 kV to several hundred volts after electrical breakdown. The voltage and current waveforms for one pulse are shown in Figure 5. This particular power supply was manufactured by SRL under a government contract and was not a commercially available power supply.

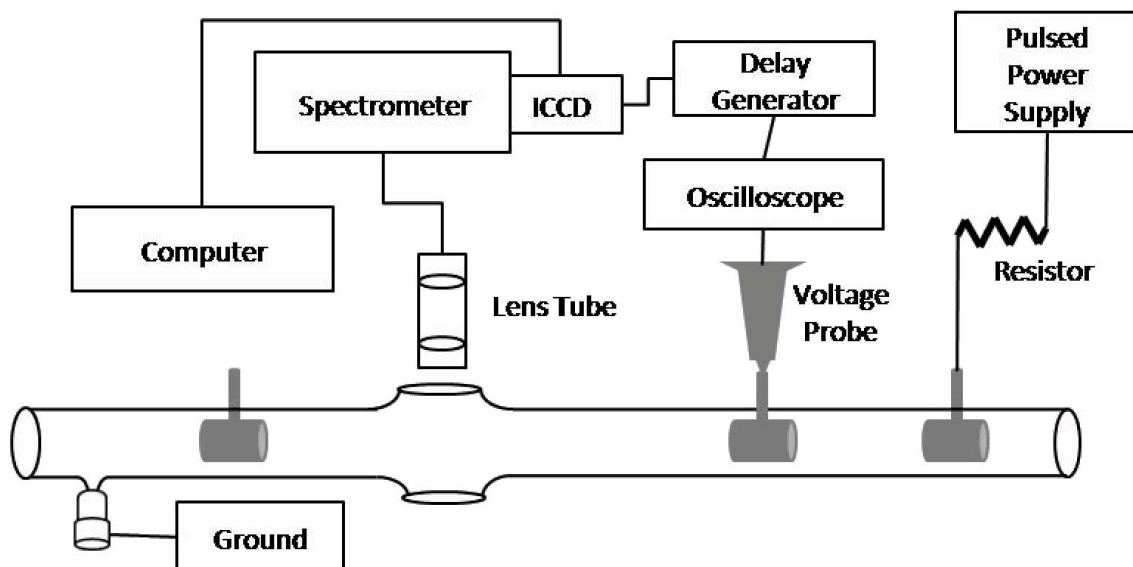


Figure 4: Optical Emission measurement set Up

5.1.3 Pressure and Flow Measurement

A model 127 MKS baratron head, positioned along the metal vacuum pipes midway between the quartz outlet tube and the drag pump, measured the pressure up to 1 torr. The glass and metal tubes connecting the discharge tube to the baratron had diameters that were chosen to be relatively large so that the pressure gradient due to flow constriction was minimal and the baratron reading would accurately represent the pressure within the entire discharge tube. Ultra high purity Argon (99.999%) flowed from the cathode end of the discharge tube through the system at all times via a 20 sccm MKS type 1179 flow controller. A type 146 MKS vacuum gauge measurement and control system monitored the baratron pressure reading and signaled the proper gas flow to the flow controller, which was regulated at 1.3 sccm to maintain a pressure of 5 ± 1 mTorr.

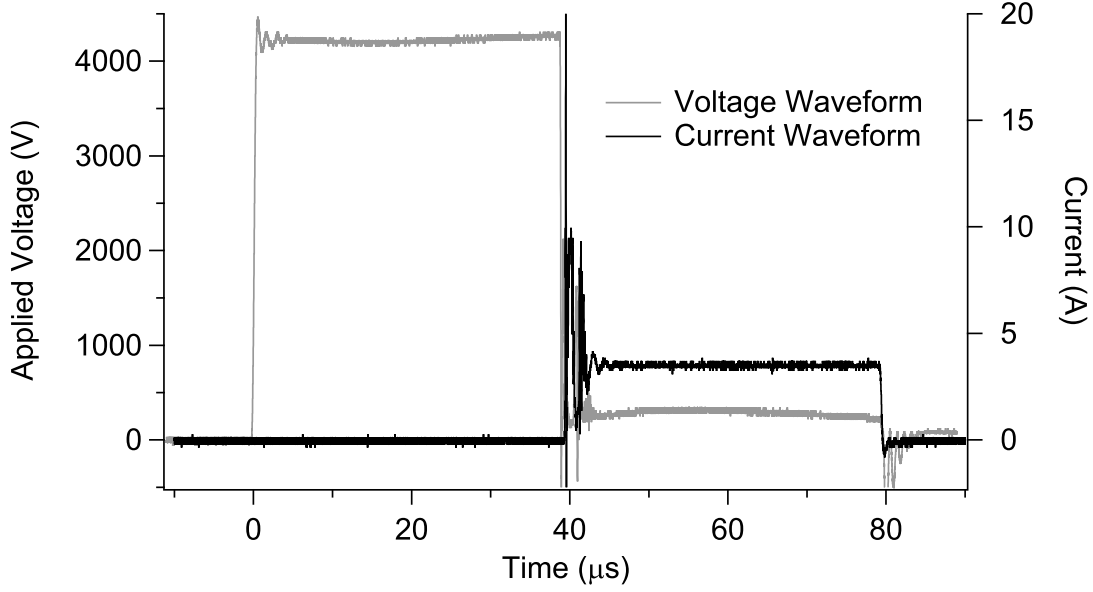


Figure 5: Voltage and current waveforms for one pulse

5.1.4 Electric Field Measurement

The E/N of the discharge in the emission region, where E is the electric field and N is the concentration of neutral particles, was calculated by measuring the potential difference between two metal probes spanning the optical detection region. Tektronix P6015 Voltage Probes were placed on two of the metal probes 10 cm apart along the discharge tube and the voltage difference was displayed on a LeCroy Waverunner LT334 oscilloscope. For calibration, both Tektronix probes could be placed on a single metal probe to ensure that the difference between the voltage waveforms from each Tektronix probe as a function of time was minimized near zero. The uncertainty in the voltage difference measurement was fairly large because the initial 4 kV applied voltage required a measurement probe with high-voltage tolerance even though the applied voltage dropped considerably after breakdown. During periods of transient voltage, such as the beginning of the applied voltage pulse and discharge breakdown, an accurate measurement of the voltage difference was essentially impossible due to the slight difference in the time response of the probes. Therefore, accurate voltage difference measurements were accomplished only during periods of relatively constant applied voltage, such as the time during the discharge but well after breakdown. These different time periods of either transient or relatively constant voltage can be easily seen in Figure 6 which displays the voltage waveforms of both of the high voltage probes. During a typical discharge, the resulting voltage difference of 80 V was near the limit of resolution for the Tektronix P6015 Voltage Probes and the assigned uncertainty of the voltage difference measurement was ± 20 V. As shown in Figure 7, during the discharge "on" period, a voltage difference of 80 ± 20 V over a 80 cm metal probe separation ($E=1$ V/cm) was measured within a typical 5 ± 1 mTorr ($N=1.6 \times 10^{14} \text{ cm}^{-3}$) discharge which resulted in an E/N of $(6 \pm 2) \times 10^{-15}$ V.

cm^2 or $600 \pm 200 \text{ Td}$, where $1 \text{ Td} = 10^{-17} \text{ V cm}^2$. Immediately after a typical discharge the voltage difference was also measured but the lower voltages at this time resulted in a higher percent uncertainty. As seen in Figure 7, immediately after the discharge, a voltage difference of $15 \pm 5 \text{ V}$ over the 80 cm probe separation resulted in an E/N of $(1.2 \pm .5) \times 10^{-15} \text{ V} \cdot \text{cm}^2$ or approximately $120 \pm 50 \text{ Td}$.

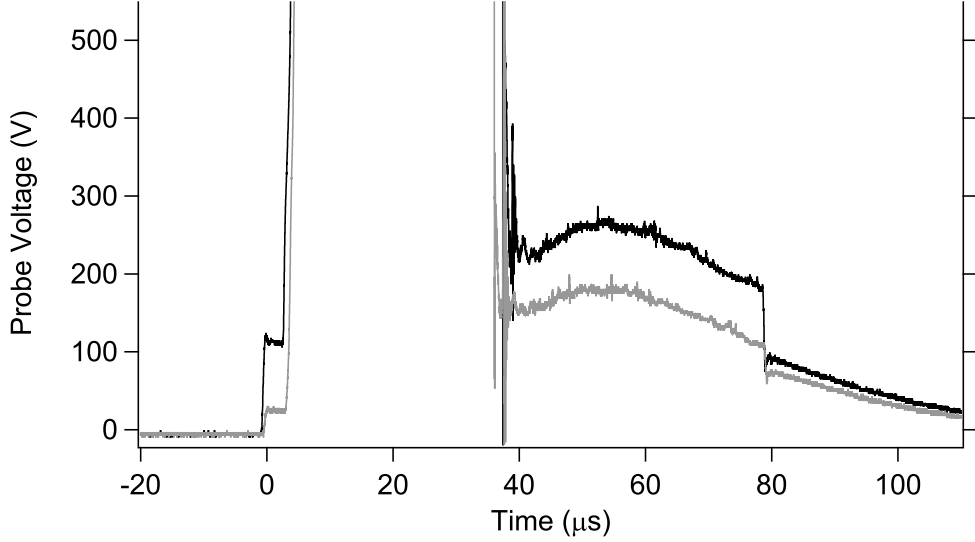


Figure 6: Voltage probe measurements

5.1.5 Optical Emission Measurement

For the spectral analyses of optical emission from the Ar discharge, light was collected and focused into a fiber-optic coupled spectrometer and imaged by an intensified charged coupled device (ICCD) camera. Radially directed optical emission from the discharge was collected through a 5 cm flat window on the radial wall of the quartz tube and passed through two collection lenses in series, as shown in Figure 4. The light was collected and collimated first by a 5 cm diameter, 9 cm focal length converging lens and then focused onto an optical fiber with a 5 cm diameter, 11 cm focal length converging lens. A 4 m fiber optic cable transmitted the emission light to the front slits of a 0.5 m focal length Acton 500i spectrometer with an imaging Czerny-Turner optical design with aspheric mirrors. The emission light was dispersed within the spectrometer with a $68 \text{ mm} \times 68 \text{ mm}$ grating with 1200 grooves per mm and a blaze wavelength of 300 nm and had a rated resolution of 0.05 nm at 435.8 nm with a $10 \mu\text{m}$ entrance slit. The resulting spectrum at the output aperture of the spectrometer was imaged by an Andor iStar 712 ICCD camera with an active imaging area of $18.4 \text{ mm} \times 18.4 \text{ mm}$ consisting of 512×512 imaging pixels and a spectral range of 115 nm to 920 nm [60]. The image intensifier included a microchannel plate that provided a minimum of 500 counts per

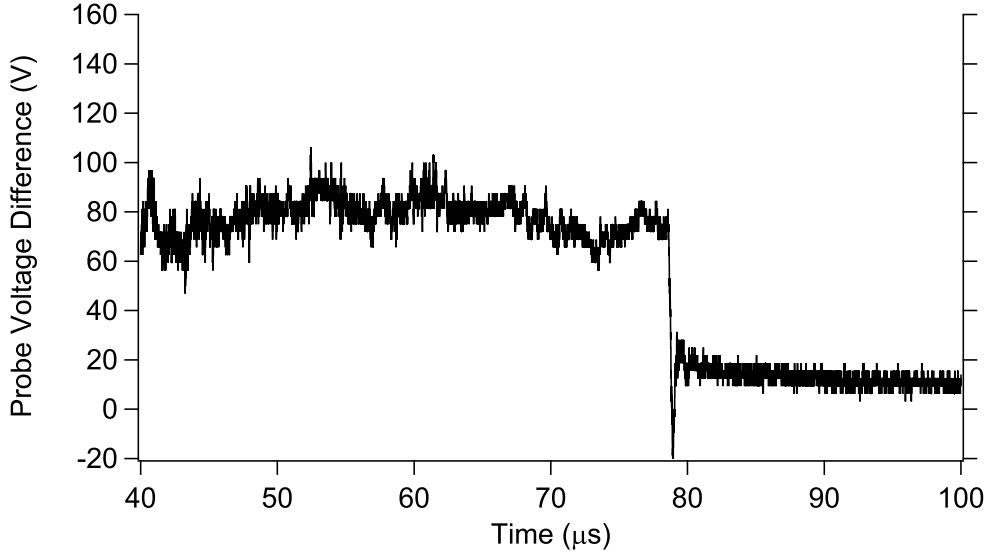


Figure 7: Difference in voltage probe measurements

photon amplification at full gain setting. The minimum optical gate width of the ICCD camera was 2 ns, although in these experiments the gate width was typically set to 500 ns, which provided both sufficient temporal resolution and adequate total image counts. In this work, the spectrometer gratings imaged a spectrum on the ICCD array that was centered at 420 nm and spanned a total spectral range of 16 nm across the 512 horizontal pixel columns. The data from the ICCD camera was fed through a computer mounted PCI controller card and processed by the Andor iStar computer program. The program produced a line spectrum by integrating over the horizontal pixel columns and assigning intensities to the corresponding wavelengths associated with the horizontal pixels.

The quantum efficiency of the ICCD camera and grating efficiency of the spectrometer varied little over the spectral range studied in this work, between 412 and 428 nm. The combined changes in efficiencies resulted in an intensity change of less than 1% over this optical range. Since much larger uncertainties were introduced when simulating the emission spectra, the total experimental optical detection efficiency was considered constant as a function of wavelength and no calibration factor was applied to the experimental emission spectral data.

The optical gate delay and gate width were parameters of the ICCD camera that needed to be controlled in order to collect the emission light at various times throughout and after the 80 μ s voltage pulse. For system triggering purposes, the pulsed power supply served as the master source which triggered the LeCroy oscilloscope through the voltage rise on one of the Tektronix voltage probes. The "trigger output" of the oscilloscope was then sent to the trigger input of a Stanford Research Systems model DG535 delay generator. A TTL signal from the delay generator was lastly sent to the external trigger input of the ICCD camera. This set the ICCD optical gate delay of zero to correspond with the start of the voltage pulse and, in most cases, before complete electrical breakdown and

significant emission occurred. The gate delay could be adjusted by the user in the Andor iStar program to control when the ICCD camera began to collect emission light during or after the pulse. The Andor ICCD camera was also capable of averaging data counts over multiple voltage pulses in order to improve resolution of the spectrum lines. The parameter in the Andor iStar program that controlled the amount of averaging was the number of accumulations. For this experiment, 1000 accumulations provided sufficient data averaging to create a highly resolved line spectrum.

Since this was a pulsed system, the discharge properties would slightly change with each voltage pulse and the electric field and metastable densities at one specific time for one pulse may be slightly different at the same time for another pulse. In general, this difference was small, the jitter between pulses was approximately 100 ns, but it did make it difficult to get a precise measurement during certain times in the discharge. For example, it was difficult to get a precise measurement of emission light when breakdown occurred since a large change in emission light occurred over this short amount of time. To compensate for this, the gate width for each acquisition was set at 500 ns and the number of counts was accumulated over 1000 voltage pulses.

The Ar gas flow of 1.3 sccm at 5 mTorr itself was not sufficiently large to insure that absolutely all of the Ar metastables from the previous pulse were removed before the start of the next pulse, although other loss mechanisms such as diffusion to the walls combined with the flow should cause this left-over density of metastables to be negligible. This assumption was confirmed with laser diode absorption measurements described later.

5.2 Absorption

Diode laser absorption spectral analysis was used to verify the metastable density calculations stemming from the optical emission measurements within the pulsed dc discharge. A New Focus Vortex 6013 continuous tunable diode laser produced approximately 6 mW of infrared radiation and had the capability to adjust laser frequency over an 80 GHz range. The specific model of the Vortex 6013 used here was centered at a laser frequency of 388008 GHz, or an air wavelength of 772.421 nm, and had a frequency range that included both the $1s_3 \rightarrow 2p_2$ and $1s_5 \rightarrow 2p_7$ transitions in Ar at 388008 GHz and 388031 GHz respectively. From the resulting absorption spectrum over these two transitions, the absolute densities of both the $1s_3$ and $1s_5$ metastables could be calculated as discussed in section 3.6. The narrow line width of the diode laser, which was less than 300 kHz [61], insured that instrumental broadening in the absorption spectrum was negligible compared to the doppler broadened line shapes of the $1s_3 \rightarrow 2p_2$ and $1s_5 \rightarrow 2p_7$ transitions, which were on the order of 800 MHz. The laser frequency was adjusted by using an input analog voltage signal to control a piezo-electric actuator within the diode laser head. The general beam path of the diode laser involved an initial 50% beam split, with one beam reflected into a calibration etalon and the other beam transmitted through the Ar pulsed discharge and onto a silicon photodiode as shown in Figure 8.

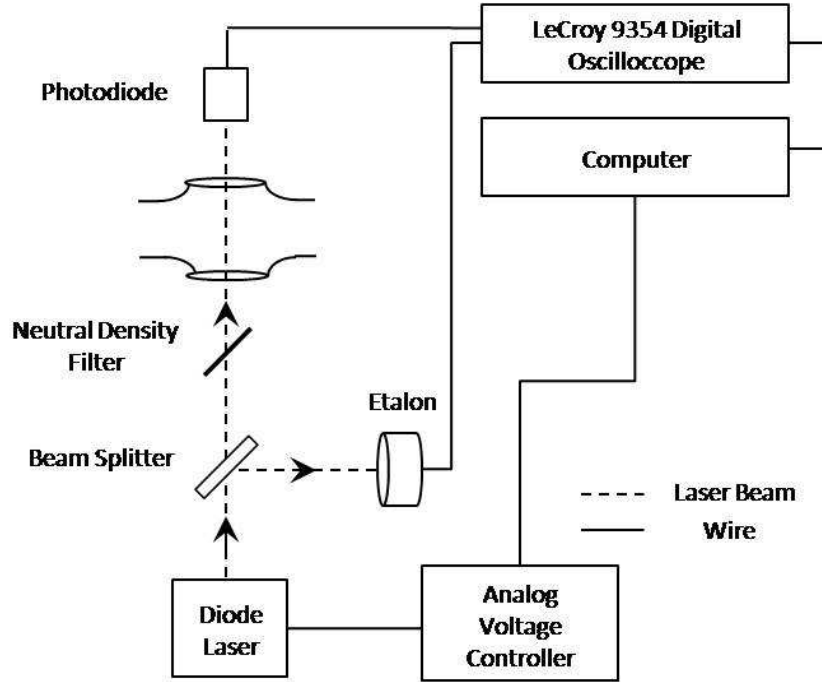


Figure 8: Diode laser absorption experimental set up

Since the laser frequency did not necessarily scale linearly with the input analog voltage signal, a Burleigh 2 GHz free spectral range etalon was used to track the relative frequency change as the analog voltage was ramped. The interference of the reflected laser beam within the etalon produced an output transmission signal that was periodic with laser frequency and resulted in peak transmission every 2 GHz. As the input analog voltage was ramped, this periodic etalon signal allowed precise calibration of the analog voltage to the laser frequency.

The beam that was transmitted through the beam splitter was directed through a series of neutral density filters to insure that excess laser power did not saturate the Ar absorption transitions of interest. With excess laser power, the rate of absorption to the upper state may become larger than the spontaneous rate of emission from that state. This would cause the overall line shape of the absorption spectrum to broaden, which is a saturation effect termed power broadening. Neutral density filters were added until the observed absorption spectral line shape was unaffected by greater filtering, which indicated the absence of power broadening due to saturation.

From the filters, the beam traveled into the Ar discharge through the 5 cm flat window on the radial wall of the quartz tube, which was the same window through which light was collected in the optical emission experiments. The quartz tube was mounted on a vertical translation stage so that the vertical position of the beam passing through the window could be adjusted, which would allow an analysis of the radial profile of the metastable density. After passing through the discharge, the laser beam exited the quartz tube through a second 5 cm flat window on the opposite wall and was directed

into a PDA55 amplified silicon detector. The silicon detector produced an output signal proportional to laser power by a factor of 235 V/mW, although all that was necessary for this analysis was a relative laser power measurement, since the transmission ratio I/I_o was the ultimate parameter required.

Both the etalon output signal and the silicon detector signal were sent to a LeCroy 9354C digital oscilloscope. Similar to the emission measurements, the pulsed power supply acted as the master source and directly triggered the oscilloscope, which made the etalon and silicon detector waveforms be directly related in time to the applied voltage pulse. The oscilloscope displayed a temporal profile of the laser power reaching the detector either with no discharge or any time relative to a $80\mu\text{s}$ pulse discharge. This allowed a baseline measurement of I_o when no discharge was present and a relative value of I could be found before, during, or after a pulse discharge. This resulted in an I/I_o value corresponding to a specific time relative to the pulse discharge. An example of the temporal profile of the transmission ratio, I/I_o , at resonant frequency for the $1s_5 \rightarrow 2p_7$ transition is shown in 9. The final transmission spectra, from which the primary temperature and metastable density calculations were made, each consisted of a set of I/I_o values, all taken at the same time relative to the $80\mu\text{s}$ pulse discharge, as a function of laser frequency. A LabVIEW based program controlled the ramping of the analog voltage to scan the laser frequency and controlled the data acquisition to record the I/I_o transmission spectrum as a function of the ramped analog voltage. The change in voltage was then related to the change in laser frequency using the etalon signal, which allowed the transmission spectra to be plotted against frequency. An example

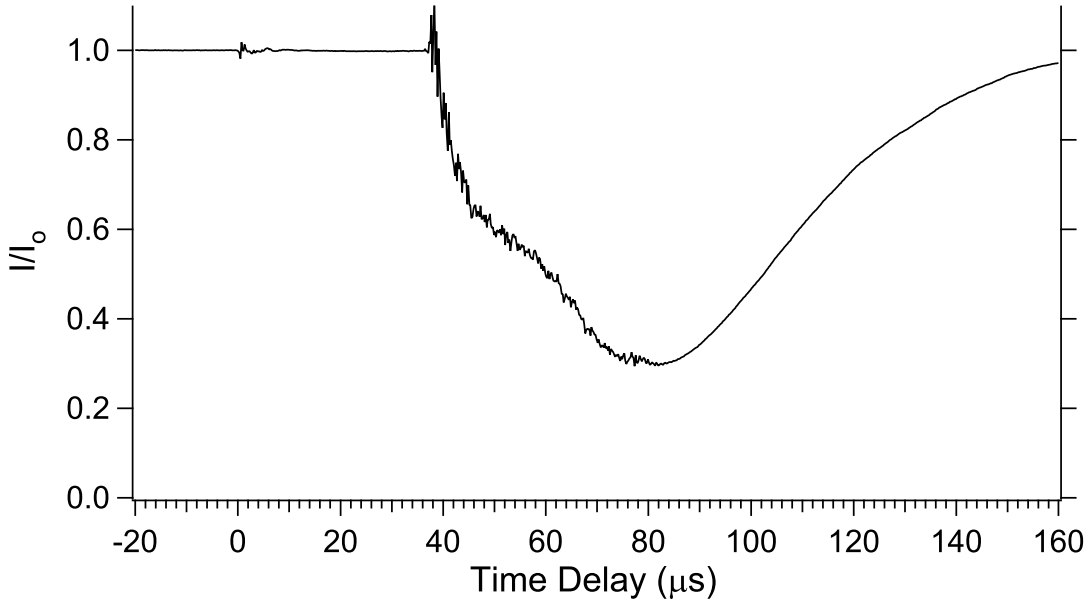


Figure 9: Transmission ratio vs time

transmission spectrum along with the calibrated etalon signal are plotted against relative frequency in Figure 10, which shows the two absorption peaks corresponding to the $1s_3 \rightarrow 2p_2$ and $1s_5 \rightarrow 2p_7$ transitions in Ar. The Doppler widths were experimentally determined by analyzing the I/I_o transmission spectrum from Figure 10, which was taken during the discharge when absorption, and therefore metastable density, was high. By taking the natural log of the entire transmission spectrum, the Doppler width could be found by fitting $\ln(I_o/I)$ with a gaussian fit function as shown in equation 3.27 in section 3.6. The Doppler width, $\Delta\nu_d$, values for the $1s_3 \rightarrow 2p_2$ and $1s_5 \rightarrow 2p_7$ transitions were measured to be 802 MHz and 815 MHz respectively, as shown in Figures 11 and 12, which corresponded to Ar gas temperatures of 330 K and 340 K. This indicated that the gas temperature during the discharge was only slightly higher than room temperature and therefore the measured $\Delta\nu_d$ was assumed to be valid as well for interpreting absorption measurements during breakdown and after the discharge, since the temperature at those times should also be near room temperature. An effective gas length parameter, l , over

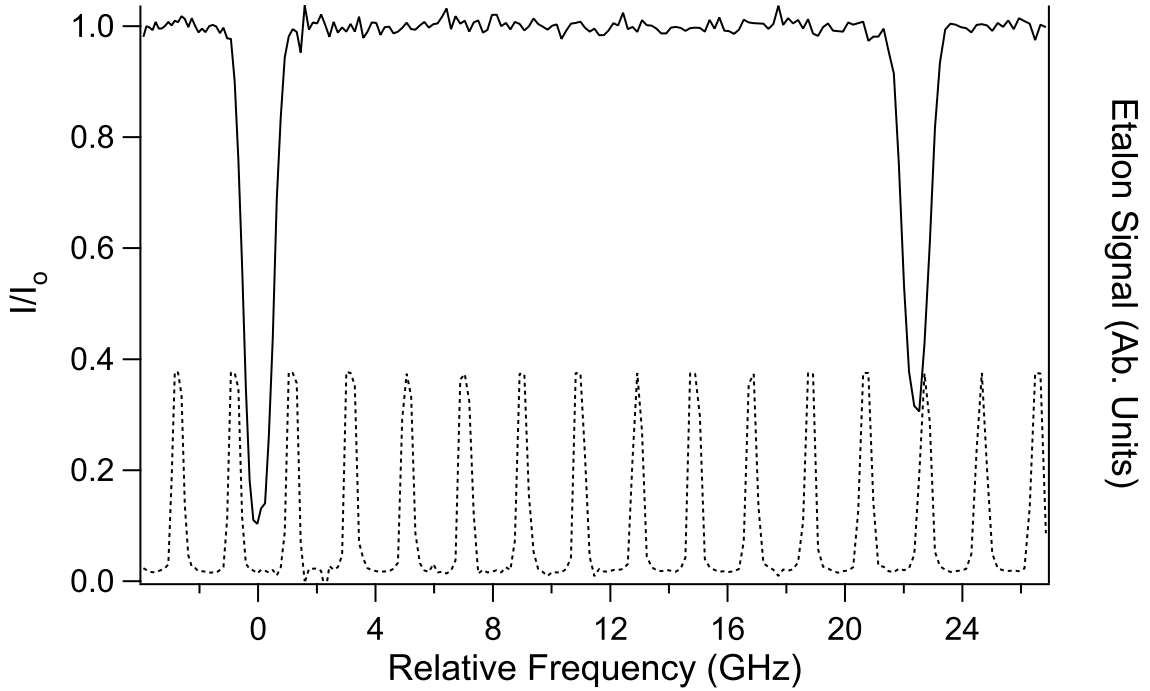


Figure 10: Transmission (solid line) and etalon signal (dotted line) vs relative Frequency

which N^* could be assumed uniform, was determined for use in equation 3.28. A radial profile of N^*l column density measurements were conducted at various vertical positions through the discharge tube and are shown as crosses in Figure 13. The results indicate that the column density is generally concentrated within a 2 cm diameter volume at the center of the tube and drops off quickly towards the wall outside of this diameter. Therefore an effective gas length of $l=2$ cm was assigned to be used in calculations using

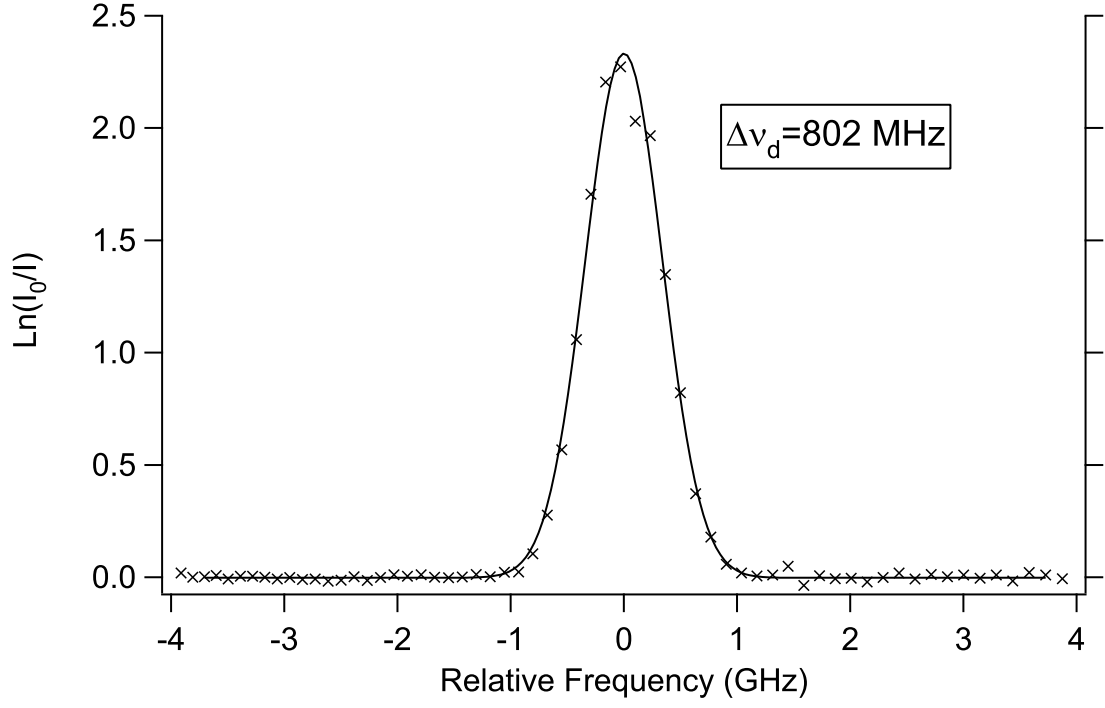


Figure 11: Gaussian fit (solid line) and $\ln(I_o/I)$ (\times) for $1s_3 \rightarrow 2p_2$ transition

equation 3.28 and represents a column length of reasonably uniform metastable density such as shown in Figure 13 by the dotted outline.

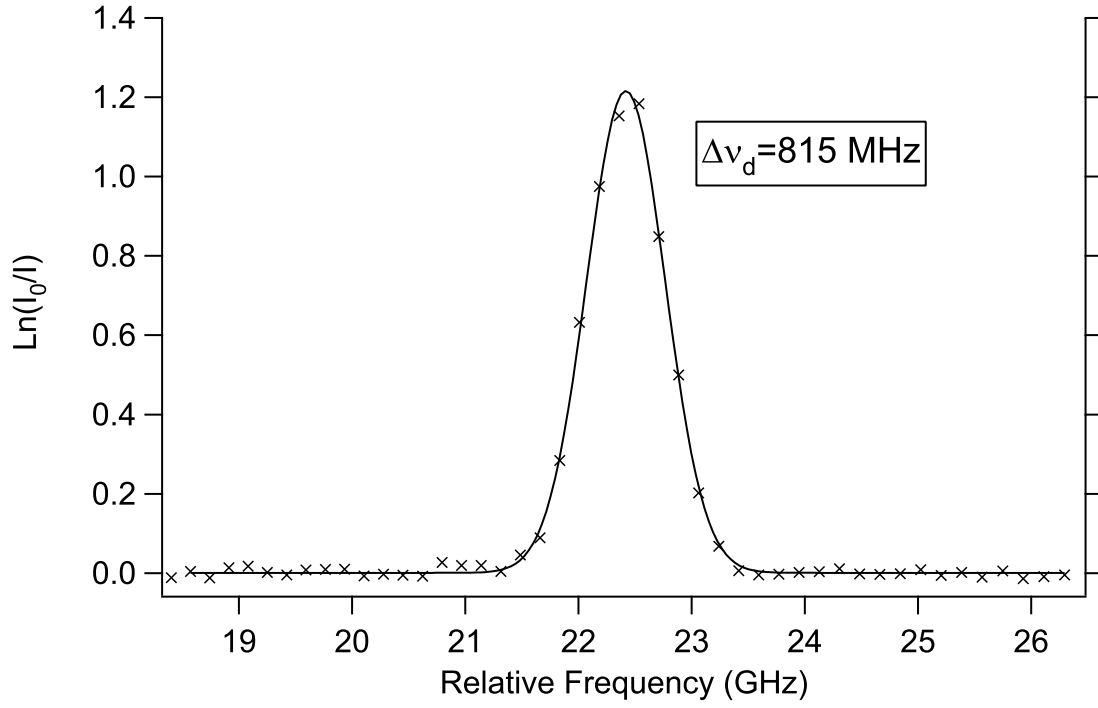


Figure 12: Gaussian fit (solid line) and $\ln(I_o/I)$ (\times) for $1s_5 \rightarrow 2p_7$ transition

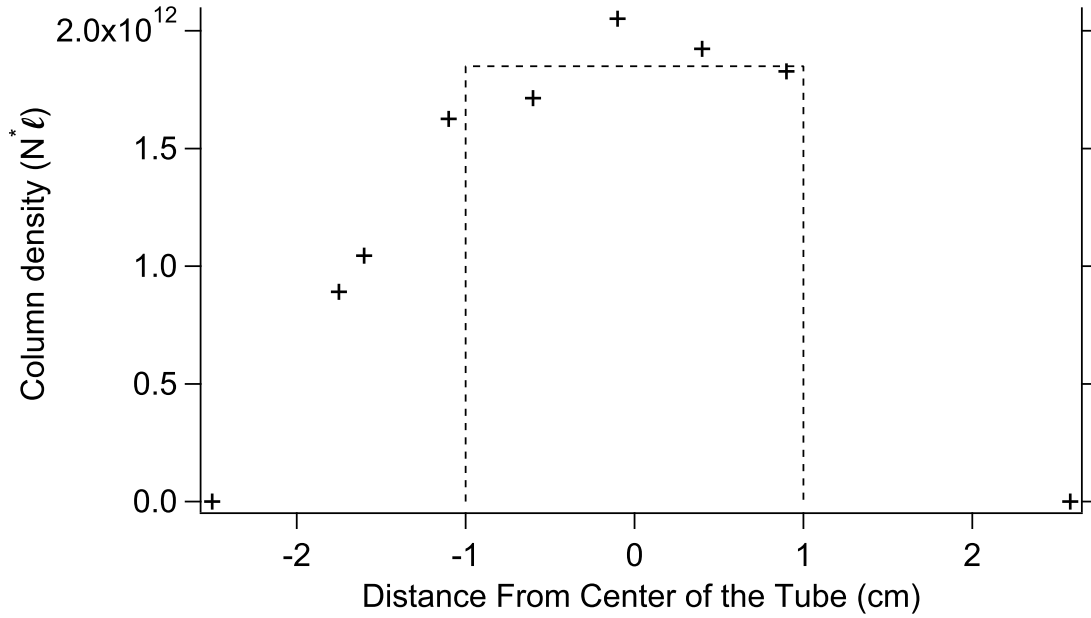


Figure 13: Column density measurements

CHAPTER 6

Results and Discussion

6.1 Experimental Emission Spectra

Emission from the Ar discharge tube was recorded at select times throughout the dc pulse. Three short windows in time were selected to represent three extreme variations in the emission line intensity distribution due to stark changes in either the EEDF and/or the ratio of metastable to ground state number densities, N^*/N , during the discharge pulse. These three select times are shown in Figure 14 and represent (i) during breakdown, (ii) during the discharge, and (iii) immediately after the discharge.

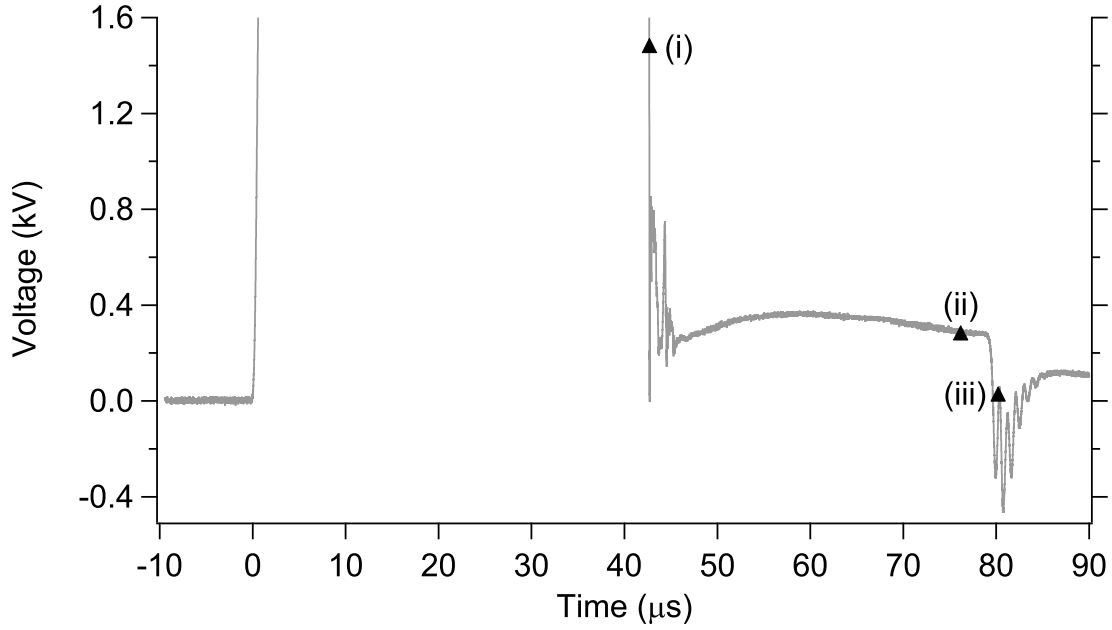


Figure 14: Times where emission was recorded

Figures 15, 16, and 17 show the raw experimental data of the relative emission intensities between 412 nm and 429 nm for the three select times in an Argon pulsed discharge at 5 mTorr.

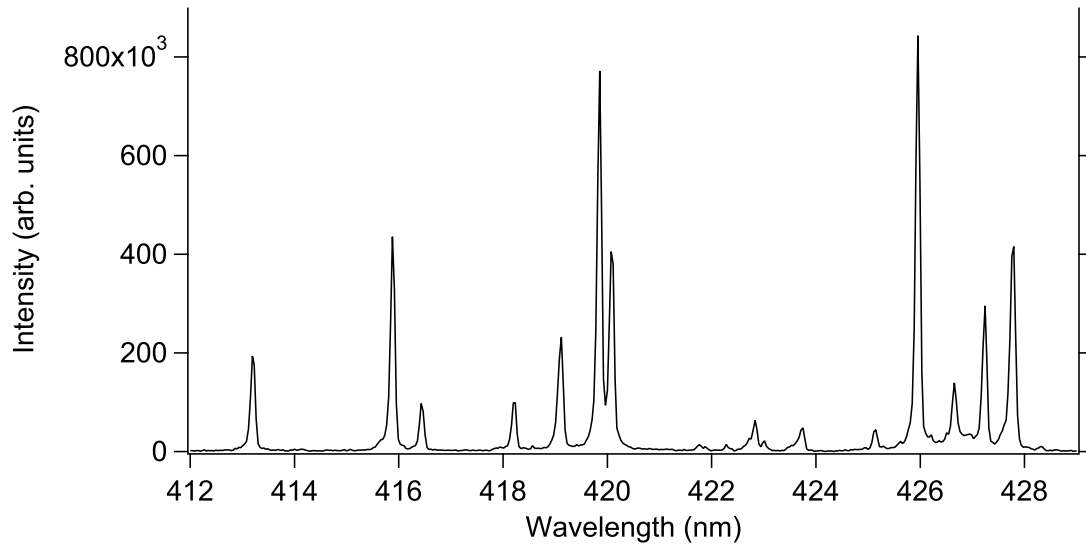


Figure 15: Emission during breakdown

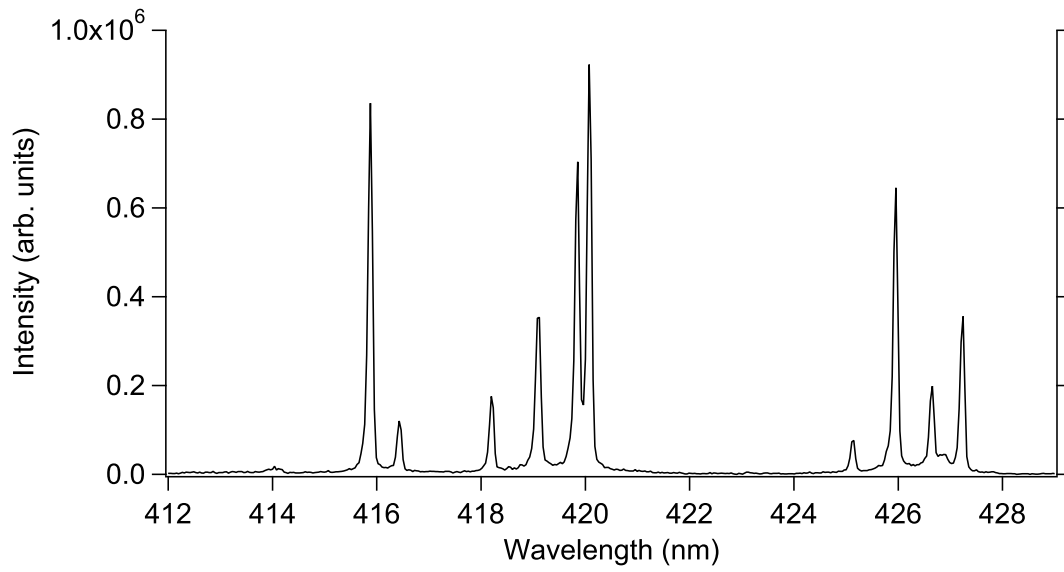


Figure 16: Emission during discharge

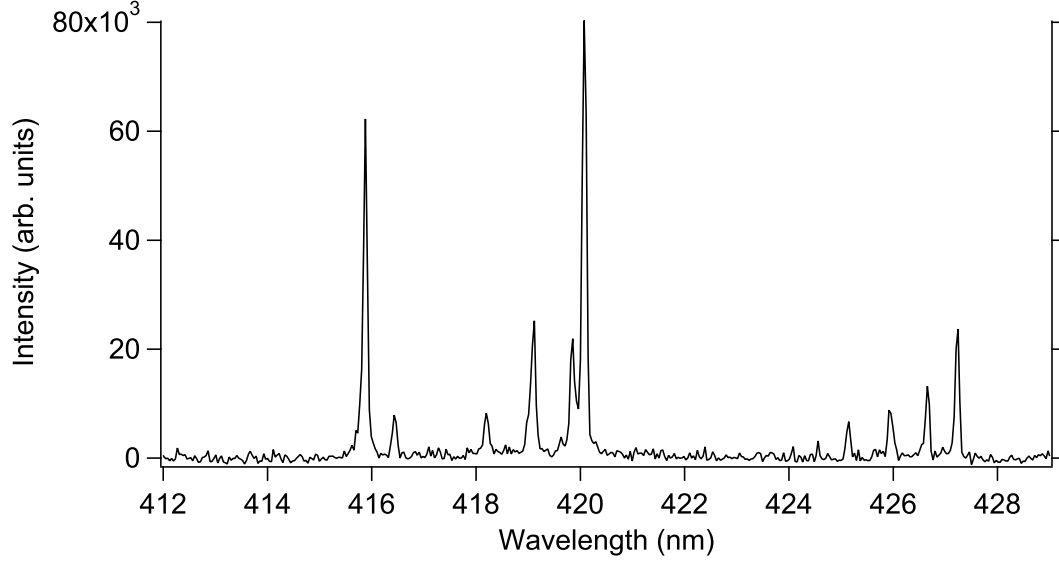


Figure 17: Emission after discharge

The following is a brief initial discussion of the general differences in appearance of the spectral lines in the three experimental plots without reference to atomic states or electrical discharge parameters. The most noticeable differences in the three spectra include the presence of known ion emission lines at 413.2, 422.8, 423.7, and 427.8 nm occurring only in Figure 15 during breakdown and also the relative changes between two other notable groups of emission lines in Figures 15, 16, and 17 for each select time. One of these groups include the strong emissions lines at 419.8 nm and 426.0 nm while the other includes strong lines at 420.1 nm and 416.0 nm. The similar quantum transitional characteristics of these groups of lines will be discussed in detail later. For convenience, the 420.1 nm line and the 419.8 nm line will be representative of their respective groups in these discussions. During breakdown, along with the presence of the ion emission lines, the 419.8 nm line is observed in Figure 15 to be significantly more intense than the 420.1 nm line, which is an observation not readily reported in Ar discharges. During the discharge, the 420.1 nm line in Figure 16 is now clearly more intense than the 419.8 nm line and no ion emission lines are observed. Immediately after the discharge, Figure 17 shows that the 420.1 nm line has increased its relative intensity to the 419.8 nm line compared to emission during the discharge.

6.2 Simulated Emission Spectra

Each of the three experimental emission spectra can be fitted with simulated spectra of relative emission generated from equation 3.17. As discussed in section 3.5, the relative emission intensity is a strong function of N^*/N and the EEDF, so these values must be

provided to generate a simulated spectrum. For clarification of this discussion, equation 3.17 is re-written below

$$I_{em}(\lambda)_{relative} = \sum_{n,m} \frac{\delta(\lambda_{nm})}{\lambda_{nm}} \int_0^\infty \left[\sigma_{nm}(\epsilon) + g_i \frac{N^*}{N} \sigma_{nm}^*(\epsilon) \right] \epsilon f(\epsilon) d\epsilon, \quad (6.1)$$

The comprehensive set of experimental data of $\sigma_{nm}(\epsilon)$ and $\sigma_{nm}^*(\epsilon)$ for Ar compiled by Lin et al. ([11],[20],[23]) and used in this study to generate simulated spectra using equation 6.1 are shown in Figure 18. For a detailed description of the set of cross sections used in this work, refer to appendix ???. These represent the cross sections corresponding to radiative transitions in the 412 nm to 429 nm range which include $3p \rightarrow 1s$ neutral Ar emission lines as well as several Ar ion emission lines. It is important to note that some values of $\sigma_{nm}^*(\epsilon)$ are on the order of 100 times larger than $\sigma_{nm}(\epsilon)$, but, as shown in equation 6.1, $\sigma_{nm}^*(\epsilon)$ is multiplied by $g_i N^*/N$, which greatly reduces the $I_{em}(\lambda)_{relative}$ contribution from metastable excitation, often to the extent of being comparable to the ground state excitation contribution.

As discussed in section 3.4, the EEDF, $f(\epsilon)$, can be calculated from a user provided E/N value for a steady state case where the electric field and electron distribution is approximately stationary in time. It is clear through trial that it is not possible to obtain unique fits of $I_{em}(\lambda)_{relative}$ to the experimental spectra by varying both the N^*/N and the EEDF input parameters, so some additional experimental evidence or assumptions was needed to generate unique fits. The general approach to provide the additional information to achieve fits at all three select times was, for time (i) to assume that $N^*/N=0$ during breakdown and investigate the EEDF that corresponds to the best fit, for time (ii) to assign an E/N corresponding to a voltage difference measurement during the discharge and allow the N^*/N to vary for the best fit, and finally for time (iii) to assume that N^*/N immediately after the discharge is unchanged from the N^*/N calculation at time (ii) and allow E/N to vary for the best fit. For any combination of EEDF and N^*/N , a proportionality constant c , which scales the simulated relative emission lines, $I_{em}(\lambda)_{relative}$, to experimental emission lines, $I_{em}(\lambda)_{experimental}$, was determined by minimizing the χ^2 value of the form

$$\chi^2 = \sum_{em} [(c \times I_{em}(\lambda)_{relative} - I_{em}(\lambda)_{experimental}) \times w_{em}]^2, \quad (6.2)$$

where w_{em} was a weighting factor that was proportional to the experimental intensity, and \sum_{em} represented the sum over all simulated emission lines. The minimum χ^2 for any single combination of EEDF and N^*/N was then compared to other combinations where either the EEDF or N^*/N were varied until the lowest χ^2 was found.

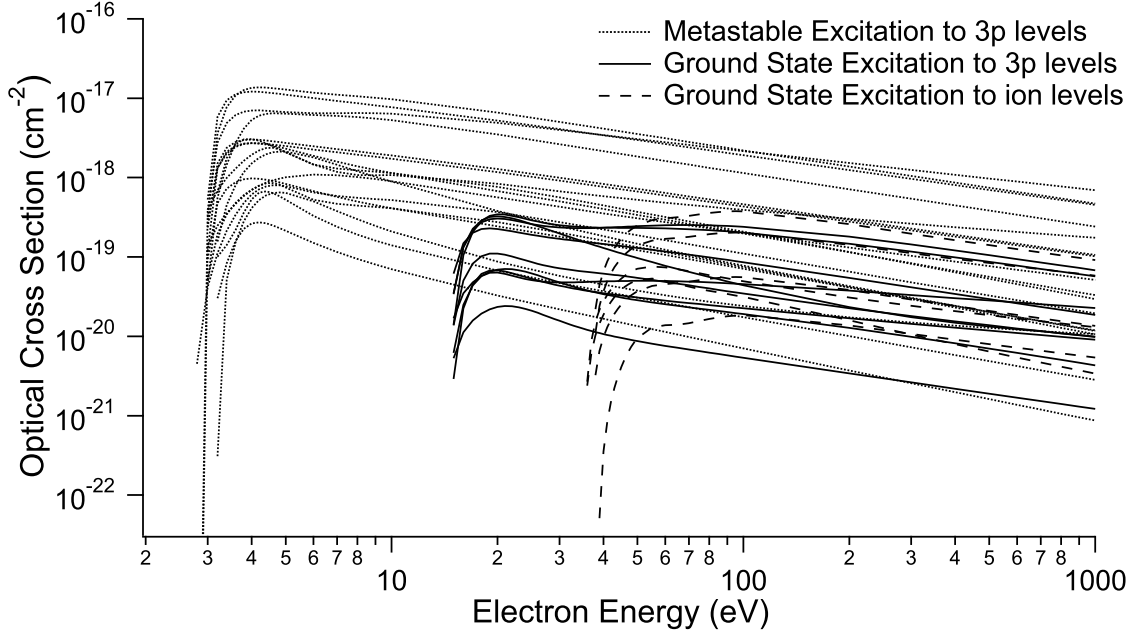


Figure 18: Cross sections used in theoretical fit

6.2.1 Simulated Spectrum During Breakdown

For the case during breakdown at time (i), a value of $N^*/N=0$ was assigned in equation 6.1, because the discharge had just been initiated and it was assumed that the long-lived metastables had not had sufficient time to build in density. This $N^*/N=0$ assumption was verified through diode laser absorption measurements and will be discussed in detail later. The EEDF during breakdown could not be considered a steady state case since the electric field and electron density were changing rapidly during this period of time. The experimental voltage difference measurement in Figure 6 is also not useful in determining a E/N during breakdown due to uncertainties in relative response times and triggering of the probes during this time of transient electric field. Thus, a user provided E/N measurement and BolSig EEDF calculation was not used in this case during breakdown. The experimental emission provided some evidence of the EEDF as Ar ion emission lines were observed during breakdown, indicating the presence of a significant high energy EEDF component. In lieu of solving the Boltzmann equation for time (i), an approximated EEDF was generated to represent the higher energy distribution and provide a fit to the observed trends in the experimental emission data. A simple Boltzmann distribution was used as the approximate EEDF and applied to equation 6.1 to create a simulated spectrum. This EEDF was in the form

$$f(\epsilon) = Ae^{-\epsilon/kT} \quad (6.3)$$

where kT represents the electron temperature in units of eV. The best fit of the experimental data during breakdown corresponded to a kT of 20 eV. Considering the unknown nature of the EEDF in this non steady state case, the electron temperature of 20 eV has a significantly large uncertainty, but seems a reasonable value for an applied voltage dropping from several thousand to several hundred volts in 5 mTorr of Ar. The simulated spectrum corresponding to a kT of 20 eV and $N^*/N=0$ is shown in Figure 19 along with the experimental emission data during breakdown.

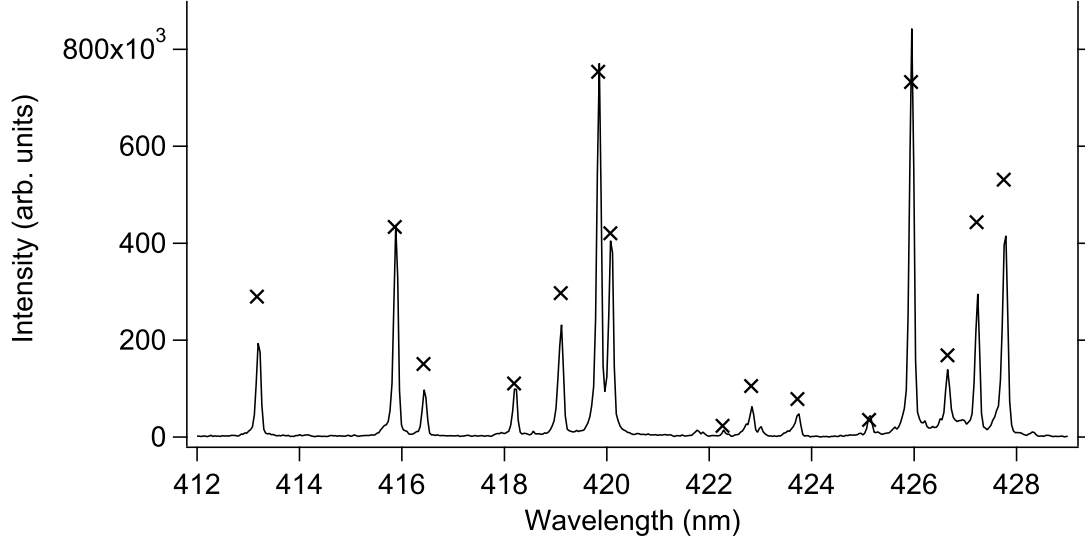


Figure 19: Emission at time (i) and simulated fit (\times)

A comparison of the simulated and experimental spectra shows a reasonably good fit of all of the Ar transition lines represented in the electron impact cross section data set. The small discrepancies seen between some of the lines could be expected given the approximate nature of the EEDF due to the transient electric field over the 500 ns observation period and the uncertainty in triggering over multiple pulses. Specifically, the fit was impressive for the unusual ratio between the 420.1 nm and the 419.8 nm lines which was 1 : 1.9, or 0.5. The origin of this notably low ratio of 420.1 nm to 419.8 nm line intensity can be clearly seen in Figure 20 where the energy distribution of electrons can be compared to select cross sections representing direct and step-wise excitation. In this graph the EEDF is in the form $\epsilon f(\epsilon)$ to better relate the EEDF to equation 6.1.

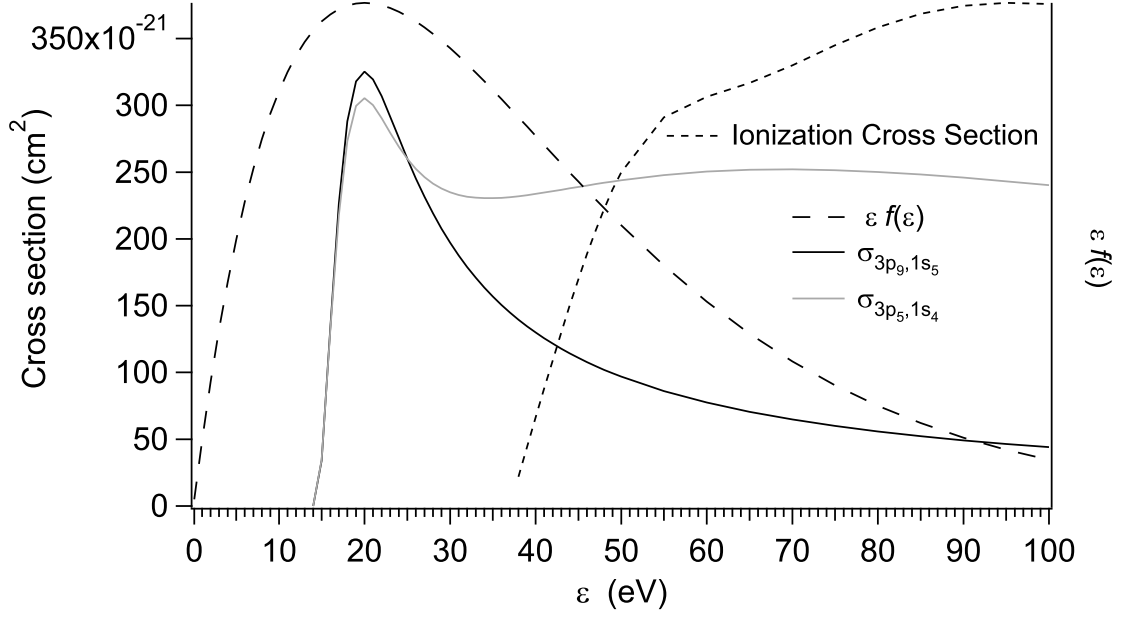


Figure 20: $\epsilon f(\epsilon)$ at time (i) and optical cross sections

Plots of the Ar direct excitation cross sections $\sigma_{3p9,1s5}$ and $\sigma_{3p5,1s4}$ corresponding to the 420.1 nm and 419.8 nm line emissions respectively are also shown in Figure 20. The two direct excitation cross sections are seen to be approximately equal for electron energies up to 25 eV, while for higher electron energies, $\sigma_{3p5,1s4}$ has a greater value which would lead to more emission at 419.8 nm in the presence of electrons with ϵ greater than 25 eV. This is clearly the case with less intense emission at 420.1 nm than 419.8 nm observed experimentally during breakdown in Figure 19. Private communications with Drs. Lin and Boffard at the University of Wisconsin revealed that such a ratio of 420.1 nm and 419.8 nm emission is unusual and not readily reported [62], most likely due to the uniqueness of capturing the Ar emission solely during the breakdown period of a pulsed discharge when the E/N is high and N^*/N is low. In further considering the assumption of $N^*/N=0$, it was found that for the EEDF with $kT=20$ eV, the fit of the simulated emission spectrum would noticeably change to an increase in N^*/N on the order of 0.001, or 0.1%. This reinforces the assumption that N^*/N is negligibly small, although a more definitive analysis of the metastable density during breakdown was done using laser absorption and will be discussed later. A single Ar ionization cross section plot corresponding to the 427.75 nm ion emission line is also shown in Figure 20 which is representative of the ionization cross section set used in the analysis with threshold energies around 38 eV. As seen in this figure, the EEDF has a substantial distribution of electrons with energies above 38 eV and thus the observation of ion emission would be expected as was observed in the experimental emission spectrum during breakdown. With closer inspection it is seen that the intensity of the ion lines of the simulated spectrum at 413.2, 422.8, 423.7, and 427.8 nm, are generally a little higher than the experimental values but the relative intensities between the four ion lines are accurate.

This over-calculation in the simulated ion emission spectrum is likely due to the actual EEDF not being an exact Boltzmann distribution function as was approximated in this model.

6.2.2 Simulated Spectrum During Discharge

For the case during the discharge at time (ii), the electron density and electric field were assumed to reach steady state and therefore the E/N could be determined from a measurement of the voltage difference between two metal probes spanning the optical detection region. The average voltage difference measurement in Figure 7 combined with pressure measurements made during the discharge, as discussed in section 5.1.4, gave an E/N value of 600 ± 200 Td. A Bolsig calculation for Ar at 600 Td generated the theoretical EEDF. By inputting the EEDF as $f(\epsilon)$, and the electron impact cross sections as $\sigma_{m,n}$ and $\sigma_{m,n}^*$, and then using N^*/N as an independent variable, the best fit of $I_{em}(\lambda)_{relative}$ from equation 6.1 to the experimental emission intensity data in Figure 16 was determined with a least squares fit. The best fit of the simulated spectrum to the peaks in the experimental spectrum during the discharge at 600 Td is shown in Figure 21 which corresponded to a best fit N^*/N of $0.007 \pm .003$, or 0.7%.

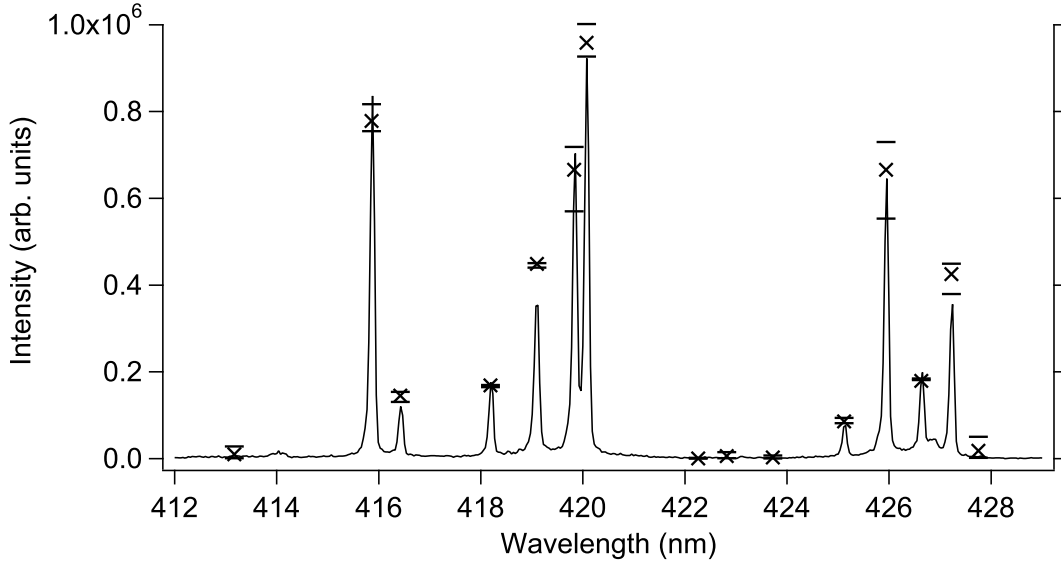


Figure 21: Emission at time (ii) and simulated fit (\times) with error bars

A comparison of the simulated and experimental spectra during the discharge shows a good fit for most transition lines within the 400 nm range. The fit was particularly good for the ratio between the 420.1 nm and the 419.8 nm lines which was 1.3 : 1. This observed ratio of 1.3 : 1 agrees fairly well with the theoretical prediction by Boffard et al. of a 1 : 1 ratio for a Ar discharge with significant direct excitation. The major cause

of uncertainty in the simulated emission spectrum results from the large uncertainty in the voltage difference measurement. The error bars shown for the simulated emission represents the effect of ± 200 Td uncertainty on each simulated transition peak. The large range in uncertainties for the various peaks was due to the variation in shape and threshold of the cross sections as a function of energy, leaving certain transition intensities more susceptible to changes in E/N than others. In contrast to most of the simulated emission lines, the line at 419.1 nm had a simulated value in excess of 20% more than the experimental value. The 419.1 nm experimental peak intensity lay outside the simulation error bars, which were very small as the simulated relative intensity at 419.1 nm was not as sensitive to E/N changes as were other lines. This disagreement between the experimental and simulated relative intensities at 419.1 nm was consistent throughout the 3 time periods studied in this work. This consistent disagreement likely indicated some unresolved uncertainty for the 419.1 nm transition in this experiment or in the previously published measurements of the cross sections used in the simulated fit.

The origin of the slightly more intense 420.1 nm emission than 419.8 nm can be explained by the presence of Ar 1s metastables and the resulting electron impact step-wise excitation from these metastable states. This can be shown graphically in Figure 22, where the EEDF for 600 Td is plotted along with 4 select cross section plots representing direct and step-wise excitation leading to both 420.1 nm and 419.8 nm emission. No ion cross section plots are shown since very little ion emission was observed due to the ion excitation threshold of approximately 38 eV and the lack of high energy electrons in the EEDF at 600 Td. The step-wise excitation cross sections from the metastables in Figure 22 have been multiplied by $g_i N^*/N$ to represent the relative effect that the metastables have on $I_{em}(\lambda)_{relative}$ in equation 6.1. It is clearly seen that the overlap of the EEDF with the lower energy step-wise excitation cross sections, $\sigma_{n,m}^*$, is much greater than the overlap with the higher energy direct excitation cross section from the ground state, $\sigma_{n,m}$. It is also the case for $\sigma_{n,m}^*$ in Figure 22, that $\sigma_{3p_9,1s_5}^*$ which emits at 420.1 nm, is generally several times larger than $\sigma_{3p_5,1s_4}^*$ which emits at 419.8 nm. This combination leads to clear excess emission at 420.1 nm for N^*/N and E/N parameters in the range of 0.7% and 600 Td respectively.

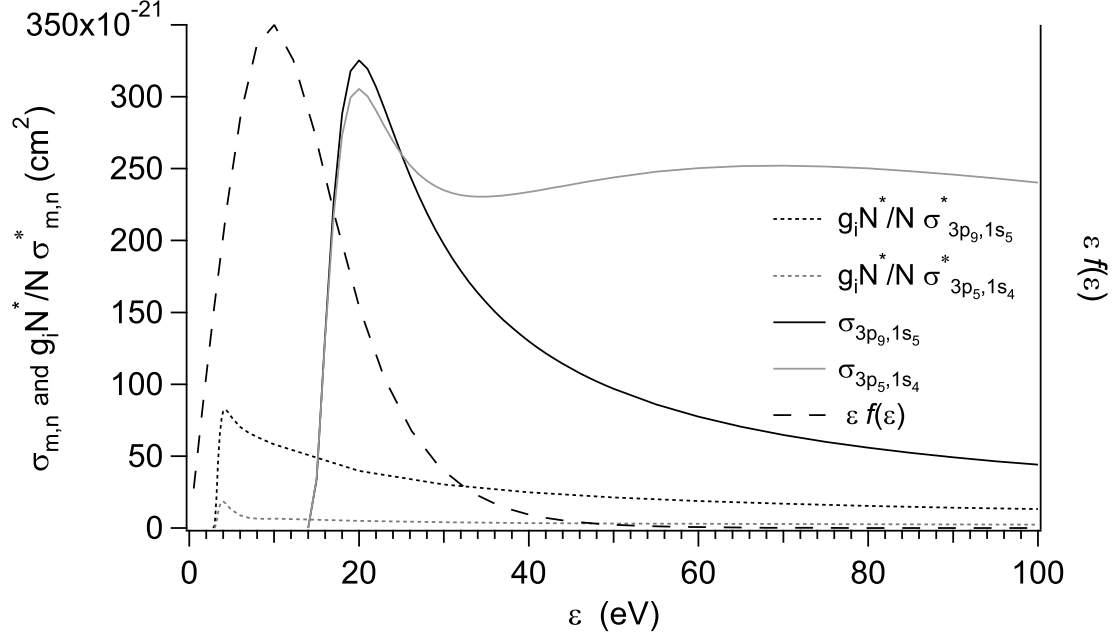


Figure 22: $\epsilon f(\epsilon)$ at time (ii) and optical cross sections

The N^*/N value of 0.7% corresponding to an absolute metastable density of $1.1 \times 10^{12} \text{cm}^{-3}$, obtained through the best fit of the simulated spectrum can be considered a reasonable value for the a high voltage pulse discharge in low pressure Ar. Comparing previous measurements of metastable density, Hebner, in a highly referenced paper, determined a peak metastable density $1.3 \times 10^{11} \text{cm}^{-3}$ in an Ar inductively coupled plasma (ICP) at 10 mTorr of Ar by absorption spectroscopy [27]. Bogaerts et al. determined a peak metastable density of $1.5 \times 10^{12} \text{cm}^{-3}$ in an Ar DC discharge at 375 mTorr through modeling techniques [63]. More recently, Boffard et al. determined a peak metastable density of $5 \times 10^{10} \text{cm}^{-3}$ in an Ar 600 W ICP at 5 mTorr [64]. The absolute metastable density of $1.1 \times 10^{12} \text{cm}^{-3}$ in this work is in the same general range as all of the aforementioned reputable measurements, albeit taken under different discharge conditions. An alternative analysis of the metastable density during the discharge was also done using laser absorption, which confirmed the general magnitude of the density calculation and will be discussed later.

6.2.3 Simulated Spectrum After Discharge

For the case immediately after the discharge at time (iii), the electron density and electric field were decaying rapidly with time toward zero. The emission measurement was taken within $1 \mu\text{s}$ of the termination of the applied voltage and the emission intensity at this time was rapidly decaying as the discharge was entering an "afterglow" state. Although the E/N was greatly reduced compared to during the discharge, it was assumed that

the metastable density had not change significantly over the short time period. Thus, to generate the simulated spectrum from equation 6.1, N^*/N was set equal to the 0.007 value determined during the discharge and was held at that value while the best fit was determined by varying the E/N . The best fit of the simulated spectrum to the peaks in the experimental spectrum after the discharge for $N^*/N=0.007$ is shown in Figure 23 which corresponded to a best fit E/N of 130 Td. The voltage difference measurement in Figure 7 from section 5.1.4 resulted in an E/N of 120 ± 50 Td, so the best fit E/N of 130 Td is certainly within the error bars of the experiment. There was some uncertainty in the simulated spectrum due to the assumption that N^*/N remained unchanged from the measurement during the discharge. This uncertainty is not quantified here, but is assumed small and is discussed later in relation to the diode laser absorption time-based measurements of absolute metastable density. The calculated EEDF corresponding to 130 Td also includes some uncertainty since the decaying N_e and E/N created a non steady-state discharge environment to some degree. The resulting good fit of the simulated spectrum in Figure 23 provides confidence, though, that the calculated EEDF was a reasonable representation with some uncertainty, although no error bars were included.

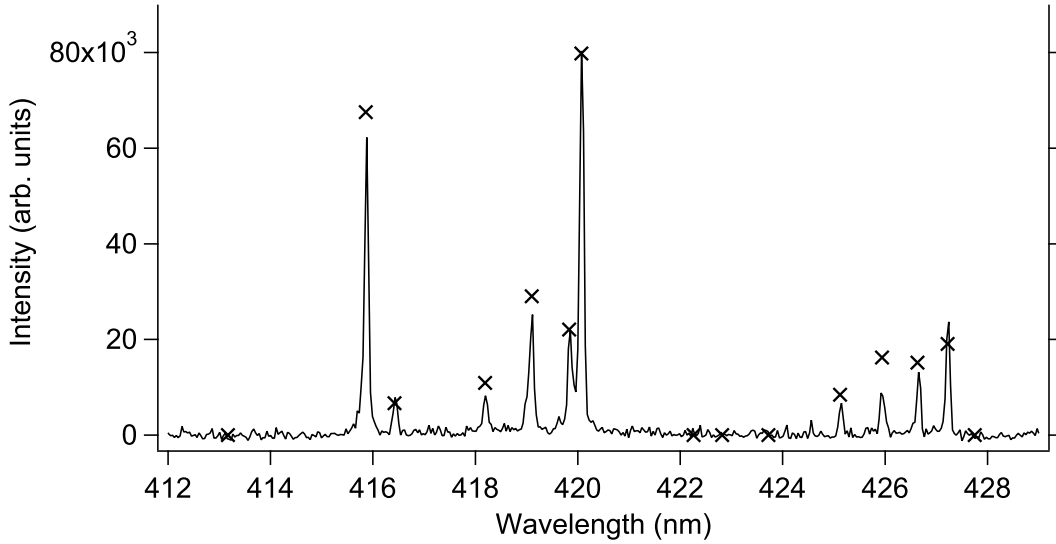


Figure 23: Emission at time (iii) with simulated fit (\times)

The absolute emission intensity in Figure 23 was significantly less than the earlier emission observations due to the decline in electron density, N_e , which leads to a proportional decrease in emission intensity, I_{em}^{nm} , as shown in equation 3.15. A comparison between the simulated and experimental peak values in Figure 23 once again shows very good agreement. Specifically the experimental and simulated relative intensities of the 420.1 nm and the 419.8 nm lines were an excellent fit with a large ratio of 3.7 : 1. This observed ratio is in excellent agreement with the measurement by DeJoseph et al. of 3.8 : 1 conducted experimentally in an Ar ICP discharge [35].

The origin of this much larger ratio of 420.1 nm emission to 419.8 nm can be attributed to a persistence of lower energy electrons causing step-wise excitation from Ar metastable states after the discharge, while a decline in high energy electrons leads to a decline in direct electron excitation. Figure 24 displays this trend after the discharge by showing the EEDF of 130 Td along with direct and step-wise cross section plots leading to both 420.1 nm and 419.8 nm emission. The graph shows the EEDF almost exclusively overlaps the step-wise excitation cross sections as the high energy tail of the EEDF indicates a very low electron density at the threshold of direct excitation. Since the plot of $\sigma_{3p_9,1s_5}^*$, corresponding to 420.1 nm emission, is seen to be consistently several times the magnitude of the $\sigma_{3p_5,1s_4}^*$ corresponding to 419.8 nm emission, this larger line intensity ratio is certainly expected when the EEDF predominantly overlaps these step-wise excitation cross sections.

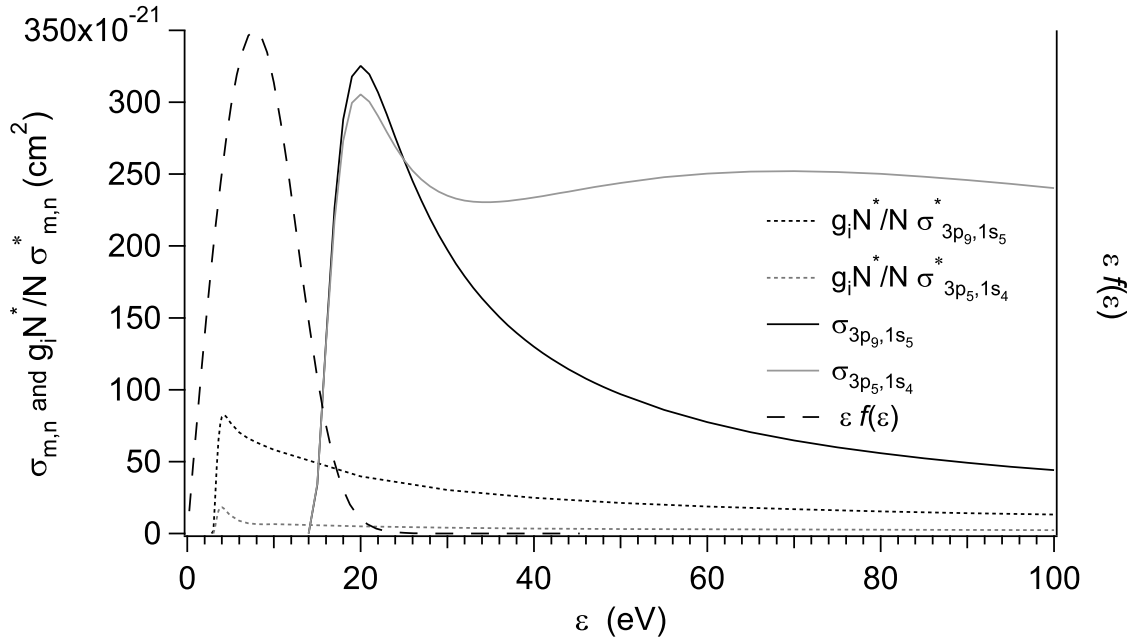


Figure 24: $\epsilon f(\epsilon)$ at time (iii) and optical cross sections

The best fit E/N of 130 Td, corresponding to an average electron energy of 7 eV, may be considered somewhat high for a typical Ar afterglow state (REF), but voltage difference measurements made after the discharge support this best fit value. The 130 Td value can be considered reasonable in this case since the emission measurement at time (iii) was made very shortly after the termination of the voltage pulse and some remnant electric field was likely present. The reason for the measurement being done so shortly after the discharge was that, at 5 mTorr Ar pressure, the emission intensity was dropping rapidly in time and was unmeasurable later in the afterglow. For higher pressure Ar discharges, which were not studied here, observable emission would last much longer after the discharge and extend the afterglow into a period where the E/N is lower.

6.3 Diode Laser Absorption

A diode laser was scanned over a range of frequencies which included the $1s_3 \rightarrow 2p_2$ and $1s_5 \rightarrow 2p_7$ transitions in Ar and an absolute metastable density was determined from the final transmission spectrum as discussed in section 5.2. An example of the temporal profile of the laser power at resonant frequency for the $1s_5 \rightarrow 2p_7$ transition is shown in 25, which shows a changing I_{peak} value during the discharge. This value corresponds to the absolute metastable number density through equation 3.28 and is re-written here for easier reference

$$N^* = \ln \left(\frac{I_o}{I_{peak}} \right) \frac{c \Delta\nu_d \sqrt{\pi}}{g_i l h\nu_o B_{12} 2\sqrt{\ln 2}}. \quad (6.4)$$

Only the $1s_5 \rightarrow 2p_7$ transition at $\nu_o=388031$ GHz was used in the calculations with eq. 6.4, because the excessive absorption of the $1s_3 \rightarrow 2p_2$ transition caused saturation effects that made it challenging to determine physical parameters. In using only the $1s_5 \rightarrow 2p_7$ transition to find the total absolute metastable density, the statistical weight factor, g_i , of 5/6 was used in equation 6.4. The Doppler width of the $1s_5 \rightarrow 2p_7$ transition was shown in section 5.2 to be $\Delta\nu_d=815$ MHz. An effective gas length of $l=2$ cm was assigned in section 5.2, which assumes a column length of uniform metastable density.

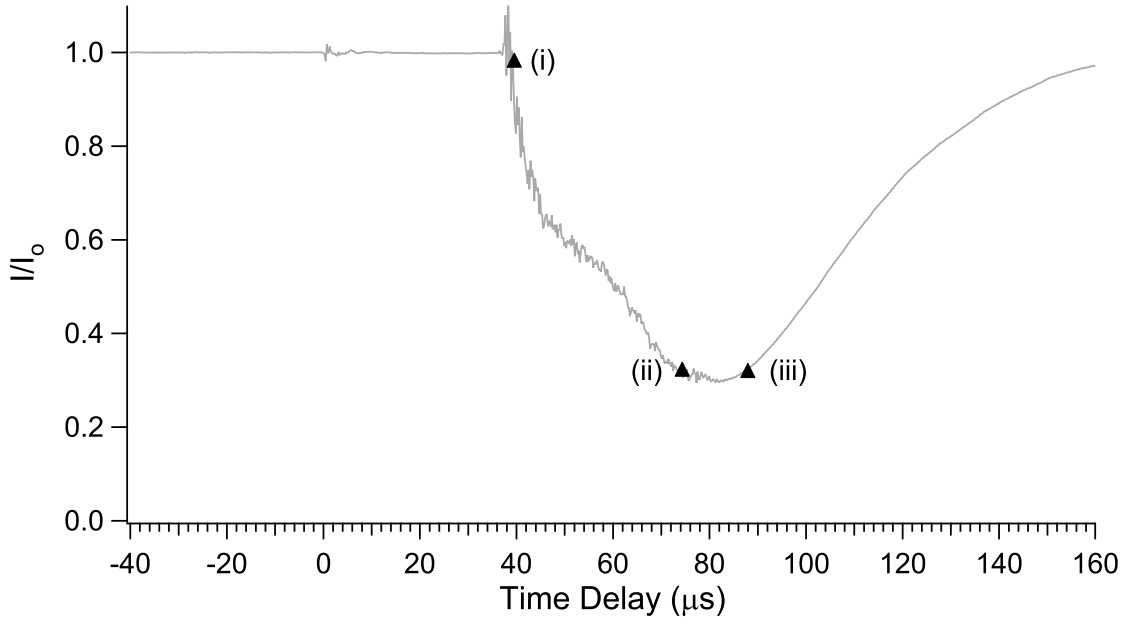


Figure 25: Temporal profile of absorption for the $1s_5 \rightarrow 2p_7$ transition

6.3.1 Absorption During Breakdown

The diode absorption signal in Figure 25 during the breakdown time period at resonant frequency was analyzed simply to confirm that the assumptions made in simulating the emission spectrum during breakdown were appropriate. Specifically, the temporal diode absorption signal was used to test the assumption that N^*/N during this time was negligible, as was assumed in the simulated emission spectrum in Figure 19. Due to the uncertainties associated with coordinating the triggering and time response of the experimental emission and absorption apparatus coupled with the low absorption signal a precise N^* value could not be derived, although an approximate N^* was determined from the absorption data and used to confirm the assumption that N^*/N was negligible. Although the signal at time (i) is relatively noisy, it is still evident that I_{peak}/I_o was no lower than 0.98 which in equation 6.4 would represent a N^* value of no greater than $1 \times 10^{10} \text{ cm}^{-3}$, or a N^*/N ratio less than 0.007%. Since it was calculated earlier in section 6.2.1 that the fit of the simulated emission spectrum during breakdown was only sensitive to an increase in N^*/N on the order of 0.1%, then the much lesser value of $N^*/N < 0.007\%$ determined through absorption verifies that setting $N^*/N=0$ was appropriate for the simulated fit. Therefore, the absorption measurements show that the metastable density during breakdown had not carried over in any significant amount from the previous discharge pulse and had not built up to a significant degree at time (i).

6.3.2 Absorption During Discharge

The diode absorption signal taken at time (ii) during the discharge was analyzed in order to compare to the absolute N^* value calculated from the simulated emission fit to the experimental emission spectrum. The measured I_{peak}/I_o corresponding to time (ii) in Figure 25 was 0.29 ± 0.02 . Using equation 6.4, this I_{peak}/I_o value resulted in an N^* value of $(8.5 \pm 0.4) \times 10^{11} \text{ cm}^{-3}$, or an N^*/N value of 0.0053 ± 0.0002 or 0.53%. This value falls within the range of uncertainty of the 0.007 ± 0.003 N^*/N value determined from emission analysis in section 6.2.2. This absolute N^* measured by diode absorption of $(8.5 \pm 0.4) \times 10^{11} \text{ cm}^{-3}$ falls within the range of $5 \times 10^{10} \text{ cm}^{-3}$ to $1.5 \times 10^{12} \text{ cm}^{-3}$ corresponding to previously published studies of Ar metastable densities, albeit under many different discharge conditions. In examining the temporal change of absorption over time during the discharge in Figure 25 it appears that N^* quickly builds after breakdown, although this rate of growth slows and varies over time and continues to grow throughout the discharge. It may be interesting in future work to examine emission at more times during the discharge and compare the results to the changing absorption signal. This would require careful analysis of the changing E/N and corresponding EEDF during these times for accurate analyses of emission spectra.

6.3.3 Absorption After Discharge

For the time (iii) period after the discharge, the diode absorption signal in Figure 25 was analyzed only to confirm that the assumption that the metastable density had not changed significantly over the short time period since the termination of the applied voltage. The emission measurement was taken within 1 μs of the termination of the applied voltage and this time period is recognizable in Figure 25 by the time scale and by the reduction in noise in the absorption signal as the discharge extinguishes. It is very clear that the absorption signal does not significantly change over the first several microseconds after the voltage is terminated. Without further calculation, this verifies the assumption that N^* immediately after the discharge is unchanged from the measurement taken during the discharge at time (ii), just prior to the voltage termination. Therefore, the value of $N^*/N=0.007$ measured from emission during discharge and used in section 6.2.2 to simulate the emission after the discharge represents a reasonable assumption. The temporal absorption signal in Figure 25 also shows the longer term rate of decay of the absorbing metastable species after the discharge was terminated and when the emission spectrum was undetectable in this 5 mTorr discharge. Analysis of this long term decay shows that the Ar metastable density, N^* , decays to one half its peak value in a time of 25 μs after the termination of the applied voltage. The decaying absorption signal also indicates that N^* is decaying to zero in a time of about 100 μs , which is much shorter than the time period of 100 ms between voltage pulses. This again confirmed that the metastable density during breakdown would not carry over in any significant amount from the previous discharge pulse.

6.4 Relation of Line-Intensity Ratio, Metastable Density, and E/N

Using equation 6.1 a graphical representation was constructed that compared the 420.1 nm to 419.8 nm line-intensity ratio, the Ar metastable density, and the E/N within the discharge for a 5 mTorr Ar discharge. This graph, shown in Figure 26, could be useful to readily determine one of these three parameters in an Ar discharge if the other two are known or could be measured. The line-intensity ratio is plotted on the y-axis and represents the calculated ratio of the 420.1 nm $3p_9 \rightarrow 1s_5$ transition to the 419.8 nm $3p_5 \rightarrow 1s_4$ transition. The N^*/N ratio is plotted on the x-axis and is the term in equation 6.1 that represents the total Ar metastable density of $1s_5$ and $1s_3$ states compared to the Ar ground state density. Each curve graphed on Figure 26 represents a specific E/N value used in BolSig to calculate the EEDF, or the $f(\epsilon)$ used in equation 6.1, which assumes a steady state case where the electric field and electron distribution are approximately stationary in time. Figure 26 also shows three specific data points, labeled as stars, corresponding to the three time periods where experimental analysis by optical emission was done.

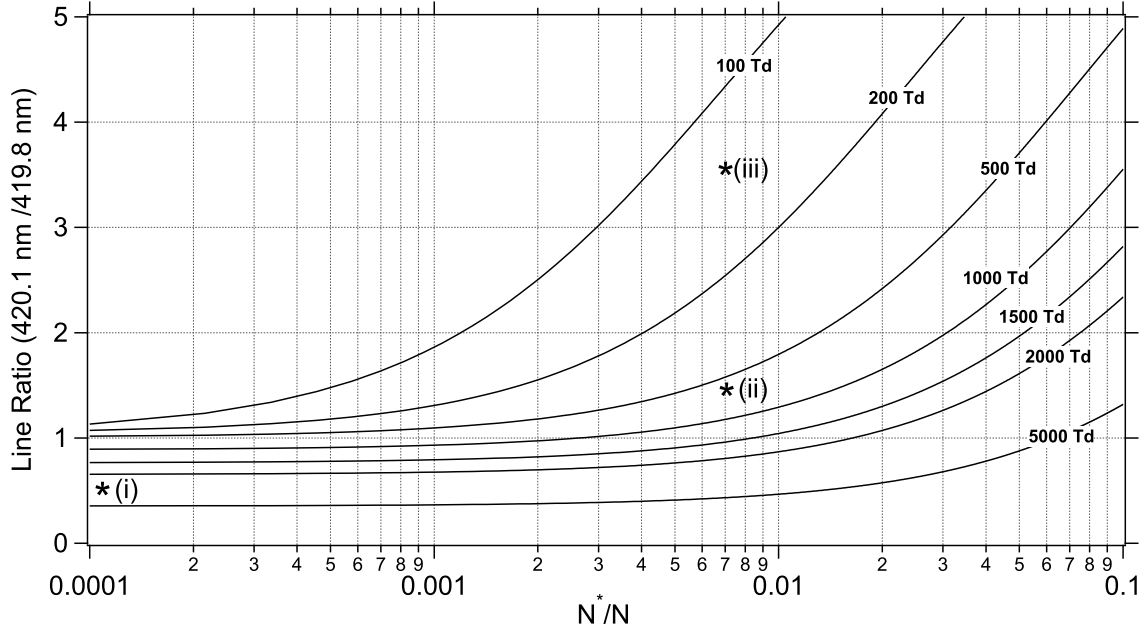


Figure 26: Graphical representation of line-intensity ratio, metastable density, and E/N

In general, Figure 26 predicts more variation in the 420.1 nm to 419.8 nm line-intensity ratio as a function of metastable density for lower E/N values. For E/N values over 1000 Td, very little variation in the line ratio is predicted for metastable densities less than 1% of ground state Ar. Since most previously published measurements of metastable densities are below 1%, the information derived from Figure 26 would be most applicable to cases of an Ar discharge with $E/N < 1000$ Td where the measured line ratio could range from 1 to 5, indicating metastable density anywhere from .01% to 1%.

For the data point on Figure 26 at time (i), during breakdown, the assumption that the metastable density was low was confirmed by absorption experiments, although this graph clearly shows that at $E/N=3000$ Td there is very little difference in the line ratio for any metastable density less than a few percent. Therefore, such a line ratio of about 1 : 1.9, or 0.5, would uniquely indicate a very high E/N around 3000 Td, but would be completely independent of the Ar metastable density below a few percent. The data point at time (ii), during the discharge, where the E/N was measured to be 600 Td is in a region of the graph where the line ratio becomes more sensitive to variations in metastable density. Therefore, it would be possible to use Figure 26 to determine metastable density for a combination of E/N and line ratio data in this region, although the difficulty and uncertainty in the E/N measurement would be the main challenge to obtaining an accurate metastable density. Figure 26 shows the measurement that was most sensitive to variations in any of the three plotted parameters was at time (iii), after the discharge. This is where the highest line ratio was measured corresponding to the lowest E/N value. In this region of the graph, small changes in E/N or metastable density can result in significant changes in the line ratio. Once again, for this graph

to be valuable to an Ar afterglow analysis, the E/N measurement would need to be accurate, which is often a challenge compared to line ratio measurements. In this work, as discussed earlier, the metastable density at time (iii) was assumed unchanged from measurements taken at time (ii) and therefore the E/N was calculated and not directly measured. In general, Figure 26 could be extremely useful in the analysis of 5 mTorr Ar discharges, although the actual application would be limited by the challenges and uncertainties in the measurements of E/N at the collection point of the optical emission.

CHAPTER 7

Conclusion

An investigation has been conducted for a 5 mTorr Ar discharge where the violet optical emission was successfully simulated by applying analytical relationships between the absolute Ar metastable concentration, the relative optical emission intensities, and the electron energy distribution. A dc pulsed discharge was used to experimentally observe the optical emission spectrum, where the Ar metastable density increased significantly during the course of the discharge pulse causing corresponding changes in the relative emission spectrum. Previously published optical cross sections, including cross sections for direct and step-wise excitation were used to relate the relative emission intensity, the Ar metastable density, and the EEDF using a theoretical model. This model, with the input of experimentally determined or assumed values, was used to generate simulated spectra which compared very favorably to experimental data.

Specifically, experimental emission spectra in the range of 412 nm to 429 nm were collected and modeled at three times relative to the discharge pulse; (i) during breakdown, (ii) during discharge and (iii) immediately after the discharge, where these three times showed distinct differences in the relative emission intensities due to the effects of direct excitation and step-wise excitation. During breakdown, the observed optical emission spectrum included the presence of ion emission lines as well as an unusually small 420.1 nm to 419.8 nm line-intensity ratio of 0.5. This line intensity ratio and the ion lines at time (i) were fitted with a simulated spectrum by assuming a negligible metastable density ($N^*/N=0$) and a Boltzmann EEDF with an electron temperature of 20 eV, which eliminated step-wise excitation and enhanced direct excitation. Although precise physical parameters were not determined by the fit during breakdown, the good fit was reassuring that the simulation model could still be representative of a high electric field situation. During the discharge, the emission intensity was generally strong, although no ion emission lines were observed. At time (ii), during the discharge, an E/N value of 600 Td was experimentally measured and a best fit parameter of $N^*/N=0.007$ produced a simulated spectrum fit to the observed optical emission spectrum. The 420.1 nm to 419.8 nm line-intensity ratio of the measurement and the simulation was 1.3, which is indicative of a mix of direct and step-wise excitation. The value of $N^*/N = 0.7\%$ corresponded to a reasonable absolute metastable density of $1.1 \times 10^{12} \text{cm}^{-3}$. Immediately after the discharge, the overall intensity of the emission was much less than during the discharge, generally decreasing in time, and the 420.1 nm to 419.8 nm line-intensity ratio had increased considerably. At time (iii), after the discharge, the much higher experimental 420.1 nm to 419.8 nm line-intensity ratio of 3.7 was fitted using the $N^*/N=0.007$ value determined during the discharge and a best fit parameter of $E/N=130$ Td. This ratio of 3.7 can be attributed to a decline in high energy electrons in the EEDF leading to a relative decline in direct electron excitation and a relative increase in step-wise excitation. Although the decaying N_e and E/N after the discharge created a non steady-state discharge environment and caused some uncertainty in the determination of the E/N ,

the spectral fit with the simulation model was still impressive and matched previously published work.

Laser diode absorption measurements were conducted which confirmed the exceptional accuracy of the absolute metastable densities either assumed or calculated in the optical emission spectral analyses. A temporal profile of the diode absorption signal included measurements taken at times (i), (ii), and (iii), corresponding to during breakdown, during the discharge, and immediately after the discharge respectively. The diode absorption signal during breakdown indicated that the metastable density N^* was no greater than $1 \times 10^{10} \text{ cm}^{-3}$, or that the N^*/N ratio less than 0.007%. This confirmed the assumption made for the simulated spectrum at time (i) that N^*/N was negligible and could be set to zero. Absorption measurements during the discharge at time (ii) resulted in $N^* = (8.5 \pm 0.4) \times 10^{11} \text{ cm}^{-3}$, or $N^*/N = 0.0053 \pm 0.0002$ or 0.53%, which falls within the range of uncertainty of the $0.007 \pm 0.003 \text{ } N^*/N$ value determined from emission analysis at time (ii). Within the first few microseconds after the discharge, the diode laser absorption signal remains relatively unchanged, which confirms the assumption of the same made for the simulated spectrum at time (iii).

A graphical representation was constructed for potential future analyses of other types of Ar discharges at 5 mTorr, which compared the 420.1 nm to 419.8 nm line-intensity ratio, the Ar metastable density, and the E/N within the discharge. Points representing the physical parameters at time (i), (ii), and (iii) were plotted as well, which graphically showed the sensitivity of each parameter to changes in the other two. In general, the graph created from equation 6.1 could hypothetically be applied to the analyses of many 5 mTorr Ar discharges, although the experimental uncertainties in the E/N measurements would make this endeavor extremely challenging under various discharge conditions. One advantage to the laboratory use of this graph is that it compares the 420.1 nm to 419.8 nm emission lines that are spectrally very close together and the efficiency of most optical detectors would vary little over such a short wavelength range.

Despite the challenges involved in accurately measuring the E/N within an Ar discharge, the results of this work in simulating violet optical emission spectra and predicting Ar metastable densities were extremely impressive. With the continuing evolution of scientific instrumentation, more affordable and accurate devices to measure E/N , optical emission line spectra, and metastable densities will enable the analysis technique presented in this work involving these three physical parameters to find widespread application in the laboratory or in industry.

REFERENCES

- [1] F. F. Chen, *Plasma Physics and Controlled Fusion*, 2 ed. (Plenum Press, New York, 1985), Vol. 1.
- [2] Y. P. Raizer, *Gas Discharge Physics* (Springer-Verlag, ADDRESS, 1991).
- [3] P. I. John, *Plasma Sciences and the Creation of Wealth* (Tata McGraw-Hill, ADDRESS, 2005).
- [4] J. J. C. Stephen M. Rossnagel and W. D. Westwood, *Handbook of Plasma Processing Technology* (Noyes Publications, Park Ridge, New Jersey, 1990).
- [5] C. Seife, *Sun in a Bottle* (Penguin Books, London, 2008).
- [6] L. J. Sandahl, Technical report, Pacific Northwest National Laboratory (unpublished).
- [7] B. N. Chapman, *Glow discharge processes : sputtering and plasma etching / Brian Chapman* (Wiley, New York :, ADDRESS, 1980), pp. xv, 406 p. :.
- [8] N. E. Small-Warren and L.-Y. C. Chiu, Phys. Rev. A **11**, 1777 (1975).
- [9] D. Mariotti, Y. Shimizu, T. Sasaki, and N. Koshizaki, Applied Physics Letters **89**, 201502 (2006).
- [10] E. Gargioni and B. Grosswendt, Rev. Mod. Phys. **80**, 451 (2008).
- [11] J. B. Boffard, B. Chiaro, T. Weber, and C. C. Lin, Atomic Data and Nuclear Data Tables **93**, 831 (2007).
- [12] J. Jonkers, M. Bakker, and J. A. M. van der Mullen, Journal of Physics D: Applied Physics **30**, 1928 (1997).
- [13] P. B. James M. Williamson and B. N. Ganguly, Jouranal of Applied Physics **97**, 103301 (2005).
- [14] L. Pauling and E. B. Wilson, in *Introduction To Quantum Mechanics With Applications to Chemistry* (Dover Publications, Inc, ADDRESS, 1935), p. 55.
- [15] L. Pauling and E. B. Wilson, in *Introduction To Quantum Mechanics With Applications to Chemistry* (Dover Publications, Inc, ADDRESS, 1935), pp. 115–134.
- [16] G. Herzberg, in *Spectra of Diatomic Molecules*, Vol. 1 of *Molecular Spectra and Molecular Structure*, 2nd ed. (Krieger Publishing Company, ADDRESS, 1950), pp. 5–29.
- [17] L. Pauling and E. B. Wilson, in *Introduction To Quantum Mechanics With Applications to Chemistry* (Dover Publications, Inc, ADDRESS, 1935), p. 230.
- [18] G. Herzberg, in *Atomic Spectra and Atomic Structure*, Vol. 1 of *Molecular Spectra and Molecular Structure* (Dover Publications, Inc, ADDRESS, 1944), pp. 126–135.
- [19] B. A. Lengyel, *Lasers*, 2nd ed. (John Wiley and Sons Inc., ADDRESS, 1971).

- [20] R. O. Jung, J. B. Boffard, L. W. Anderson, and C. C. Lin, Physical Review A (Atomic, Molecular, and Optical Physics) **75**, 052707 (2007).
- [21] J. D. Dow and R. S. Knox, Phys. Rev. **152**, 50 (1966).
- [22] J. B. Boffard, C. C. Lin, and C. A. D. Jr, Journal of Physics D: Applied Physics **37**, R143 (2004).
- [23] J. B. Boffard *et al.*, Phys. Rev. A **59**, 2749 (1999).
- [24] Y. P. Raizer, in *Gas Discharge Physics* (Springer-Verlag, ADDRESS, 1991), pp. 9–11.
- [25] G. J. M. Hagelaar and L. C. Pitchford, Plasma Sources Science and Technology **14**, 722 (2005).
- [26] G. Hagelaar, BolSig+, 2006, boltzmann-equation solver version 1.03.
- [27] G. A. Hebner, Journal of Applied Physics **80**, 2624 (1996).
- [28] R. C. Hilborn, American Journal of Physics **50**, 982 (1982).
- [29] A. E. Siegman, in *Lasers* (University Science Books, ADDRESS, 1986), p. 1186.
- [30] A. P. Thorne, *Spectrophysics* (Chapman and Hall; Wiley London, New York,, ADDRESS, 1974), pp. xiv, 402 p.
- [31] R. W. P. McWhirter, *Plasma diagnostic techniques. / Edited by Richard H. Huddleston and Stanley L. Leonard* (Academic Press, New York, :, ADDRESS, 1965), pp. xii, 627 p. .
- [32] X.-M. Zhu and Y.-K. Pu, Plasma Sources Science and Technology **17**, 024002 (2008).
- [33] M. Schulze, A. Yanguas-Gil, A. von Keudell, and P. Awakowicz, Journal of Physics D: Applied Physics **41**, 065206 (2008).
- [34] J. B. Boffard, R. O. Jung, C. C. Lin, and A. E. Wendt, Plasma Sources Science and Technology **18**, 035017 (2009).
- [35] C. DeJoseph, Jr. and V. I. Demidov, Journal of Physics B: Atomic, Molecular and Optical Physics **38**, 3805 (2005).
- [36] T. W. John Boffard, B. Chiaro and C. Lin, The Big List Argon Optical Emission Cross Sections, 2007, department of Physics, Univeristy of Wisconsin-Madison.
- [37] J. Koch and K. Niemax, Spectrochimica Acta Part B: Atomic Spectroscopy **53**, 71 (1998).
- [38] H. T. Do, V. Sushkov, and R. Hippler, New Journal of Physics **11**, 033020 (2009).
- [39] R. J. Leiweke and B. N. Ganguly, Applied Physics Letters **88**, 131501 (2006).
- [40] R. J. Leiweke and B. N. Ganguly, Applied Physics Letters **90**, 241501 (2007).
- [41] D. W. O. Heddle and J. W. Gallagher, Rev. Mod. Phys. **61**, 221 (1989).
- [42] L. G. Christophorou and J. K. Olthoff, Advances In Atomic, Molecular, and Optical Physics **44**, 155 (2001).

- [43] J. E. Chilton, J. B. Boffard, R. S. Schappe, and C. C. Lin, Phys. Rev. A **57**, 267 (1998).
- [44] J. K. Ballou, C. C. Lin, and F. E. Fajen, Phys. Rev. A **8**, 1797 (1973).
- [45] S. Tsurubuchi, T. Miyazaki, and K. Motohashi, Journal of Physics B: Atomic, Molecular and Optical Physics **29**, 1785 (1996).
- [46] T. Weber, J. B. Boffard, and C. C. Lin, Phys. Rev. A **68**, 032719 (2003).
- [47] G. A. Piech *et al.*, Phys. Rev. Lett. **81**, 309 (1998).
- [48] H. A. Hyman, Phys. Rev. A **18**, 441 (1978).
- [49] R. Srivastava, A. D. Stauffer, and L. Sharma, Phys. Rev. A **74**, 012715 (2006).
- [50] L. Sharma, R. Srivastava, and A. D. Stauffer, Journal of Physics: Conference Series **80**, 012019 .
- [51] S. Tsurubuchi, Journal of the Physical Society of Japan **66**, 3070 (1997).
- [52] I. D. Latimer and R. M. S. John, Phys. Rev. A **1**, 1612 (1970).
- [53] P. N. Clout and D. W. O. Heddle, Journal of Physics B: Atomic and Molecular Physics **4**, 483 (1971).
- [54] J. A. Sanchez, F. Blanco, G. Garcia, and J. Campos, Physica Scripta **39**, 243 .
- [55] J. A. Sanchez, J. A. Aguilera, B. Martnez, and J. Campos, Phys. Rev. A **41**, 1392 (1990).
- [56] I. P. Bogdanova and S. V. Yurgenson, Optics and Spectroscopy **62**, 21 (1987).
- [57] I. P. Bogdanova and S. V. Yurgenson, Optics and Spectroscopy **62**, 34 (1987).
- [58] I. P. Zapesochnyi *et al.*, Soviet Journal of Experimental and Theoretical Physics **36**, 1056 (1973).
- [59] I. P. Zapesochnyi, A. I. Imre, and Y. N. Semenyuk, Soviet physics, JETP **72**, .
- [60] *A User's Guide to the Andor iStar*, Andor Technology, 2001, draf Version 3A.
- [61] *Tunable Diode Laser Manual, 6000 Vortex Series*, New Focus Lasers, 2002.
- [62] C. Lin and J. Boffard, 2009, private communication.
- [63] A. Bogaerts and R. Gijbels, Phys. Rev. A **52**, 3743 (1995).
- [64] J. B. Boffard, R. O. Jung, C. C. Lin, and A. E. Wendt, Plasma Sources Science and Technology **18**, 035017 (2009).

APPENDIX

Argon Cross Section Data Set

This appendix is a review of the comprehensive set of experimental data of $\sigma_{nm}(\epsilon)$ and $\sigma_{nm}^*(\epsilon)$ for Ar which was previously compiled by Lin et al. ([11],[20],[23],[36]) and used in this study to generate simulated spectra as described in section 6.2. The energy dependent cross section is given by

$$\sigma_{nm}(\epsilon) = \sigma_{nm}(\epsilon_{Ref}) \times (q^C(\epsilon) + q^D(\epsilon)) \quad (1)$$

where ϵ_{Ref} is 50 eV for excitation from the ground state and 10 eV for excitation from the metastable states. The values $q^C(\epsilon)$ and $q^D(\epsilon)$ are

$$q^C(\epsilon) = \frac{C_1 \left(\frac{\epsilon - \epsilon_{th}}{\epsilon_R} \right)^{C_2}}{1 + \left(\frac{\epsilon - \epsilon_{th}}{C_3} \right)^{C_2 + C_4}} \quad q^D(\epsilon) = \frac{D_1 \left(\frac{\epsilon - \epsilon_{th}}{\epsilon_R} \right)^{D_2}}{1 + \left(\frac{\epsilon - \epsilon_{th}}{D_3} \right)^{D_2 + D_4}}, \quad (2)$$

where ϵ_{th} is the threshold energy, and ϵ_R is the Rydberg energy of 13.6 eV. It is important to note that $q^C(\epsilon) + q^D(\epsilon)$ are independent on the lower state of the transition. For emissions caused by excitation from the ground state, values from tables 2 and 3 can be combined to solve for the optical cross section (σ_{nm}). For emission caused by excitation from the metastable state, the constants needed to calculate the optical cross section (σ_{nm}^*) are in tables 4, 5, and 6.

Table 2: Optical cross sections for transitions originating from the ground state

Wavelength	Transition Levels	$\epsilon_{th}(eV)$	$\sigma_{mn} \text{ (cm}^{-20}\text{)}$		
			25 eV	50 eV	100 eV
413.17	$4p' \text{ } ^2P_{1/2}^o \rightarrow 4s' \text{ } ^2D_{3/2} \text{ (Ar}^+)$	37.19	-	14	20
415.86	$3p_6 \rightarrow 1s_5$	14.53	19	13	8.5
416.42	$3p_7 \rightarrow 1s_5$	14.52	5.1	5.1	4.8
418.19	$3p_2 \rightarrow 1s_3$	14.69	5.3	2.8	2.1
419.07	$3p_8 \rightarrow 1s_5$	14.51	8.6	5.0	3.6
419.1	$3p_4 \rightarrow 1s_3$	14.58	6.2	3.0	1.9
419.83	$3p_5 \rightarrow 1s_4$	14.58	26	23	20.
420.07	$3p_9 \rightarrow 1s_5$	14.5	26	10.	4.4
422.26	$5s \text{ } ^2P_{1/2} \rightarrow 4p \text{ } ^2P_{3/2}^o \text{ (Ar}^+)$	38.56	-	0.95	1.6
422.82	$4p \text{ } ^2D_{5/2}^o \rightarrow 4s \text{ } ^4P_{3/2} \text{ (Ar}^+)$	35.44	-	7.1	4.9
423.72	$4p' \text{ } ^2P_{3/2}^o \rightarrow 4s' \text{ } ^2D_{3/2} \text{ (Ar}^+)$	37.11	-	3.7	5.4
425.12	$3p_{10} \rightarrow 1s_5$	14.46	2.1	0.91	0.55
425.94	$3p_1 \rightarrow 1s_2$	14.74	29	23	21
426.63	$3p_6 \rightarrow 1s_4$	14.53	4.3	2.9	1.9
426.65	$4p \text{ } ^4D_{5/2}^o \rightarrow 4s \text{ } ^4P_{5/2} \text{ (Ar}^+)$	35.31	-	5.1	2.8
427.22	$3p_7 \rightarrow 1s_4$	14.52	15	14	13
427.75	$4p' \text{ } ^2P_{3/2}^o \rightarrow 4s' \text{ } ^2D_{5/2} \text{ (Ar}^+)$	37.11	-	25	36

Table 3: Coefficient values for $\sigma_{mn}(\epsilon)$

Level	$\epsilon_{th}(\text{eV})$	C_1	C_2	C_3	C_4	D_1	D_2	D_3	D_4
$3p_1$	14.74	9.91	1.33	4.95	1.27	0.534	1.03	40.17	0.593
$3p_2$	14.69	29.02	1.61	3.86	1.03	0.810	0.88	19.74	0.351
$3p_3$	14.69	12.94	1.22	4.48	1.61	1.125	1.06	20.06	0.571
$3p_4$	14.66	4.66	0.83	8.47	1.96	1.102	0.29	44.99	0.741
$3p_5$	14.58	6.87	1.14	4.96	1.26	0.479	1.03	50.16	0.633
$3p_6$	14.53	6.51	0.89	4.32	1.38	1.468	0.67	19.66	0.658
$3p_7$	14.52	7.46	1.25	5.00	1.70	0.910	1.35	20.05	0.312
$3p_8$	14.51	14.57	1.22	4.71	1.14	0.390	2.30	19.91	0.437
$3p_9$	14.50	26.95	1.31	4.68	0.93	2.292	-0.73	730.72	-1.046
$3p_{10}$	14.46	5.24	0.70	9.19	2.16	1.115	0.90	20.36	0.628
$\text{Ar}^+ 4p' {}^2P_{1/2}^o$	37.19	1.22	0.97	21.10	1.88	0.090	2.65	43.06	0.491
$\text{Ar}^+ 5s {}^2P_{1/2}$	38.56	1.39	1.62	17.96	2.19	0.176	2.44	43.04	0.526
$\text{Ar}^+ 4p {}^2D_{5/2}^o$	35.44	1.76	1.20	9.43	0.42	0.607	2.81	14.68	0.845
$\text{Ar}^+ 4p' {}^2P_{3/2}^o$	37.11	1.11	0.93	21.11	2.26	0.152	2.35	43.05	0.587
$\text{Ar}^+ 4p {}^4D_{5/2}^o$	35.31	1.09	1.06	20.48	2.17	0.110	1.72	46.54	0.866

Table 4: Optical cross sections for transitions originating from metastable states

Wavelength	Transition Levels	$\sigma_{mn}^*(10eV)(\text{cm}^{-18})$	
		$1s_3$	$1s_5$
415.86	$3p_6 \rightarrow 1s_5$	0	7.7
416.42	$3p_7 \rightarrow 1s_5$	0.41	0.41
418.19	$3p_2 \rightarrow 1s_3$	5.3	0.14
419.07	$3p_8 \rightarrow 1s_5$	0	1.90
419.1	$3p_4 \rightarrow 1s_3$	6.4	0.07
419.83	$3p_5 \rightarrow 1s_4$	0	1.08
420.07	$3p_9 \rightarrow 1s_5$	0	9.7
425.12	$3p_{10} \rightarrow 1s_5$	0.52	0.9
425.94	$3p_1 \rightarrow 1s_2$	0.89	0.21
426.63	$3p_6 \rightarrow 1s_4$	0	1.73
427.22	$3p_7 \rightarrow 1s_4$	1.14	1.14

Table 5: Coefficient values for $\sigma_{mn}^*(\epsilon)$ originating from the Ar $1s_5$ Metastable state

Level	$\epsilon_{th}(\text{eV})$	C_1	C_2	C_3	C_4	D_1	D_2	D_3	D_4
$3p_1$	3.19	266.00	1.68	1.43	1.21	1.535	2.85	5.78	0.198
$3p_2$	3.14	9546.70	2.83	1.08	1.62	1.889	0.18	4.01	0.784
$3p_4$	3.11	948.84	1.84	0.92	1.18	0.909	0.194	6.41	0.850
$3p_5$	3.03	348.08	1.45	0.792	1.07	16.584	3.99	6.32	0.314
$3p_6$	2.98	71.99	1.10	0.661	0.0684	2.195	0.769	4.87	0.596
$3p_7$	2.97	33.31	0.83	1.154	1.098	0.608	-0.73	8.57	-0.638
$3p_8$	2.96	82.90	1.14	0.665	0.676	2.101	0.84	5.12	0.612
$3p_9$	2.95	192.53	1.56	0.825	0.76	3.331	1.32	5.46	0.630
$3p_{10}$	2.91	15.38	1.12	1.60	0.76	17.75	1.80	2.82	0.531

Table 6: Coefficient values for $\sigma_{mn}^*(\epsilon)$ originating from the Ar $1s_3$ Metastable state

Level	$\epsilon_{th}(\text{eV})$	C_1	C_2	C_3	C_4	D_1	D_2	D_3	D_4
$3p_1$	3.02	78.37	1.42	1.76	1.49	0.345	-0.768	3.76	-1.502
$3p_2$	2.97	569.60	2.44	1.15	1.41	7.042	1.10	3.92	0.667
$3p_4$	2.94	133.04	1.42	0.684	0.554	6.165	2.11	5.15	0.449
$3p_7$	2.80	45.05	1.57	1.97	4.37	3.597	0.598	5.50	0.845
$3p_{10}$	2.74	186.41	2.13	1.74	1.95	4.338	1.19	6.10	0.745

LIST OF SYMBOLS

Chapter 2.1

Ψ	Electron wavefunction
\hat{H}_e	Hamiltonian operator for the electron wave equation
E_e	Total electron energy eigenvalue
r	Radial component of the spherical coordinate system
θ	Polar angle of the spherical coordinate system
ϕ	Azimuthal angle of the spherical coordinate system
h	Plank's constant
e	The elementary charge
Z	The number of charges on the nucleus
μ	The reduced mass of the atom
a_o	The bohr radius
L_{n-l-1}^{2l+1}	Generalized Laguerre polynomial of order n-l-1
$Y_l^m(\theta, \phi)$	Spherical harmonic of degree l and order m
m_e	Mass of an electron
l_i	The orbital angular momentum of an electron
L	The total orbital angular momentum vector
S	The total spin angular momentum vector
J	The total angular momentum vector
K	The intermediate resultant angular momentum vector

Chapter 2.2

E_n	Energy of the upper state n
E_m	Energy of the lower state m
ν_{nm}	Frequency of transition radiation between states n and m
M	Electric dipole moment
e_k	Electron charges
x, y, z	Cartesian coordinates
x_k	Electron coordinates
R^{nm}	Transition dipole moment
Ψ_m	Wavefunction of state m
Ψ_n	Wavefunction of state n
I_{em}	Intensity of emission
N	Concentration of Argon atoms
A_{nm}	Einstein coefficient
c	The speed of light
τ	Radiative lifetime of excited state n

Chapter 2.3

ϵ	Electron energy
σ_{nm}	Optical cross section originating from Ar ground state
σ_{nm}^*	Optical cross section originating from Ar metastable state

Chapter 2.4

$f(v)$	Electron velocity distribution
$-eE/m_e$	Force on the electrons applied by the electric field
Δ_v	Velocity gradient operator
C	Changes caused by collisions

Chapter 2.5

g_i	Statistical weighting factor
δ	Dirac delta function
λ	Emission wavelength

Chapter 2.6

I	Electron beam current
Δl	Section of length of the absorbing gas
N_i^*	Number density of absorbing atoms
ν	Photon frequency
B_{mn}	Einstein transition probability of absorption
$g(\nu)$	Observed line shape function
ν_o	Resonant frequency of the transition
$\Delta\nu_d$	Doppler width
k	Boltzmann constant